

Northumbria Research Link

Citation: Chen, Xue and He, Yongjun (2020) Thermo-magneto-mechanical coupling dynamics of magnetic shape memory alloys. *International Journal of Plasticity*, 129. p. 102686. ISSN 0749-6419

Published by: Elsevier

URL: <https://doi.org/10.1016/j.ijplas.2020.102686>
<<https://doi.org/10.1016/j.ijplas.2020.102686>>

This version was downloaded from Northumbria Research Link:
<http://nrl.northumbria.ac.uk/id/eprint/42274/>

Northumbria University has developed Northumbria Research Link (NRL) to enable users to access the University's research output. Copyright © and moral rights for items on NRL are retained by the individual author(s) and/or other copyright owners. Single copies of full items can be reproduced, displayed or performed, and given to third parties in any format or medium for personal research or study, educational, or not-for-profit purposes without prior permission or charge, provided the authors, title and full bibliographic details are given, as well as a hyperlink and/or URL to the original metadata page. The content must not be changed in any way. Full items must not be sold commercially in any format or medium without formal permission of the copyright holder. The full policy is available online: <http://nrl.northumbria.ac.uk/policies.html>

This document may differ from the final, published version of the research and has been made available online in accordance with publisher policies. To read and/or cite from the published version of the research, please visit the publisher's website (a subscription may be required.)

Thermo-magneto-mechanical coupling dynamics of magnetic shape memory alloys

Xue Chen^a, Yongjun He^{b,*}

^a Faculty of Engineering and Environment, Northumbria University, Newcastle Upon Tyne
NE1 8ST, UK

^b IMSIA, CNRS-EDF-CEA-ENSTA Paris, Institut Polytechnique de Paris, 828 Boulevard des
Maréchaux, 91120 Palaiseau Cedex, France

Abstract

This paper is to improve our previous phase-transformable material constitutive model (Chen et al. JMPS 2014) and implement it in a mass-spring configuration to study the recently discovered dynamic phenomena in (Zhang et al. IJP 2018a, b): the harmonic oscillator of the cyclic magnetic-field-induced deformation in Magnetic Shape Memory Alloys (MSMA) is modulated by a thermo-magneto-mechanical coupling feedback loop where the cyclic field-induced Martensite Reorientation (MR) provides cyclic dissipative deformation whose dissipation heat influencing the material temperature modifies the temperature-dependent MR process and/or triggers the martensite-to-austenite Phase Transformation (PT) to modify the martensite volume fraction so as to change the deformation oscillation amplitude. Such a feedback loop causing the amplitude modulation was ignored in the existing models. This paper develops a dynamic model to include the feedback loop by considering the heat balance (i.e. the interactions among heat generation due to MR, the latent heat release/absorption of PT and the heat transferred to the ambient), by introducing proper kinetics of the temperature-dependent MR and PT processes, and by taking into account the inertial dynamic effect with a simple mass-spring configuration. The simulation based on the model captures all the main features of the experimental phenomena and provides the relations between the macroscopic responses (the deformation amplitude and temperature evolution) and the microscopic physical mechanisms (the kinetics of MR and PT). The study reveals that, with the coupling effects, the MSMA system can be smart to keep its temperature constant by self-organized microstructures

*Corresponding author. Tel.: (+33) 169319730; fax: (+33) 169319997. E-mail address:
yongjun.he@ensta-paristech.fr (Yongjun HE)

under varying external thermo-magneto-mechanical boundary conditions. Moreover, the forward and reverse martensitic phase transformations influenced by the coupling dynamics show little hysteresis, contrasting to the usual hysteretic kinetics of the quasi-static martensitic phase transformation.

Keywords: magnetic shape memory alloys, high-frequency magnetic actuation, martensite reorientation, phase transformation kinetics, hysteresis of phase transformation.

1. Introduction

Magnetic shape memory alloy (MSMA) is a smart material exhibiting thermo-magneto-mechanical coupling phenomena. It can be actuated by temperature, mechanical stress and magnetic field. Large strain up to 10% can be achieved in the material due to the martensite reorientation and/or the martensitic phase transformation (Bruno et al., 2016; Heczko et al., 2000; Kainuma et al., 2006; Karaca et al., 2006; Murray et al., 2000; Sozinov et al., 2002; Ullakko et al., 1996). The main advantage of MSMA over the traditional shape memory alloys is its high-frequency magnetic-field-induced deformation, which makes it a promising candidate for the applications of sensors and actuators in the future (Asua et al., 2014; Hobza et al., 2018; Kohl et al., 2010, 2014; Stephan et al., 2011; Yin et al., 2016).

Some dynamic behaviours of the high-frequency magnetic-field-induced martensite reorientation have been reported in the literature. Henry (2002) measured the output strain of MSMA at the magnetic field frequency ranging from 1 Hz to 250 Hz, and found that the strain kept constant at first and then decreased when the frequency reached a threshold. Such strain decrease is due to the decrease in the magnitude of the applied magnetic field strength when increasing the frequency. The evolution of the strain amplitude with frequency observed in (Henry, 2002) was successfully simulated by Sarawate and Dapino (2008) with the Maxwell's equations which take into account the frequency effect on the field strength. Techapiesancharoenkij et al. (2009, 2011) conducted experiments at a constant magnitude of the applied magnetic field strength and found a resonance-type frequency dependence, i.e. the maximum output strain amplitude was obtained at the resonance frequency. Lai et al. (2008) observed the twin boundary motion in MSMA at various magnetic field frequencies up to 600 Hz and measured the corresponding twin boundary velocities. Faran and Shilo (2011, 2012, 2013) measured the velocities of individual twin boundary under pulsed magnetic fields and revealed different kinetic relations at high and low driving forces. They further developed a dynamic magneto-mechanical model based on the measured kinetics of twin boundary motion, and successfully simulated the resonance-type frequency-dependent response (Faran et al., 2017; Faran and Shilo, 2016). Pascan et al. (2015) measured the temperature rise of MSMA under high-frequency magnetic field, and found that both Type I and Type II twin boundaries (with different mobility (Sozinov et al., 2011; Straka et al., 2011)) can be nucleated in the dynamic loading. It is seen that all these studies were focused on the magneto-mechanical coupling behaviours of MSMA, even though some of the researchers had already recognized the strong dissipation during the high-frequency actuation and the associated significant temperature rise (e.g. Lai, 2009; Pascan, 2015; Pascan et al., 2015, 2016). The temperature rise can influence the output strain from the martensite reorientation as the driving force (so-called "twinning stress")

of the Type I twin boundary motion is sensitive to temperature (Straka et al., 2012). Such temperature rise during the actuation was usually thought to be harmful to the system's performance and should be avoided, i.e. it should not exist in the normal applications.

By contrast, recent experiments in (Zhang et al., 2018a, 2018b) focused on the thermo-magneto-mechanical coupling dynamic behaviours have systematically demonstrated how the field-induced deformation depends on the magnetic actuation, the applied mechanical stress and the thermal boundary conditions. Particularly, in the experiments, the heat exchanging rate between the MSMA system and the ambient was controlled by an airflow from a compressed air whose velocity can be tuned. Generally, with the stronger ambient airflow (i.e. higher heat exchanging rate), the system temperature would be lower as the dissipation heat can be transferred to the ambient more quickly. Interestingly, at certain ambient conditions (i.e. at a certain range of the ambient airflow velocities), the system temperature kept constant (36 °C), around the material's characteristic martensitic phase transformation temperature where both martensite and austenite phases exist in the MSMA system; that means, the field-induced Martensite Reorientation (MR) and the temperature-induced Phase Transformation (PT) can simultaneously occur, leading to a thermo-magneto-mechanical coupling loop: the cyclic MR provides dissipative deformation whose dissipation heat influencing the system temperature modifies the temperature-dependent MR process and/or triggers the martensite-to-austenite PT to modify the martensite volume fraction so as to change the deformation oscillation amplitude $\Delta\varepsilon$. Such a feedback loop leads to a non-monotonic dependence of the deformation oscillation amplitude $\Delta\varepsilon$ on the thermal condition (i.e. on the ambient heat exchange rate in Fig. 10(a)). In other words, to achieve a large dynamic deformation amplitude, we need to choose not only a proper magnetic actuation frequency (the resonance frequency), but also a proper ambient heat transfer condition.

The experimental observations and basic theoretical analysis in (Zhang et al., 2018a, 2018b) reveal the significant temperature rise due to the combined effect of the high-frequency cyclic martensite reorientation and the ambient heat exchange. To further describe the thermo-magneto-mechanical coupling dynamic behaviours (i.e. output strain and temperature evolutions) and predict the optimized working conditions of high-frequency MSMA-based actuators, a suitable dynamic model is demanded. However, the existing constitutive models of MSMA (e.g. Chen et al., 2014; Haldar et al., 2014; Kiefer and Lagoudas, 2005, 2009; Krevet et al., 2008; Morrison et al., 2008; Rogovoy and Stolbova, 2016; Wang and Steinmann, 2012; Yu et al., 2018, 2019) describe the martensite reorientation and the phase transformation separately, and cannot take into account the coupling feedback loop. In this paper, we extend

our previous martensite-reorientation model (Chen et al., 2014) to include the coupling loop by considering the heat balance (the balance between the rates of heat generation due to MR, the latent heat release/absorption of PT and the heat transferred to the ambient), by introducing proper kinetics of the temperature-dependent MR and PT processes, and by taking into account the inertial dynamic effect with a simple mass-spring configuration. The simulation based on the new model captures all the main features of the experimental phenomena and provides insights into the macro-micro relations governing the coupling dynamics. Moreover, with the aid of the model simulations, the features of the temperature-induced martensite transformation influenced by coupling dynamics are further studied.

The remaining parts of the paper are organized as follows: The extended constitutive model of MSMA and the mass-spring dynamic model are presented in Section 2. Section 3 presents the simulation results and their comparisons with the experiments. Discussions on the novel features of the coupling dynamics are given in Section 4. Section 5 is devoted to the summary and conclusions of the paper.

2. Dynamic model

2.1. Constitutive model of magnetic shape memory alloys

2.1.1. Gibbs free energy and state equations

The constitutive model is composed of two parts describing the processes of Martensite Reorientation (MR) and Phase Transformation (PT), respectively. The MR modelling is mainly based on our previous model (Chen et al., 2014) while the PT modelling is a new proposition. The studied magnetic shape memory alloy is Ni-Mn-Ga single crystal used in the experiments of (Zhang et al., 2018a). State variables in the constitutive model include the absolute temperature T , the Cauchy stress tensor $\underline{\underline{\sigma}}$, the internal magnetic field strength vector \underline{H} , the volume fraction z_0 of austenite, and the volume fractions (z_1, z_2, z_3) of the three pseudo-tetragonal 5M martensite variants, as shown in Fig. 1(a). The Gibbs free energy density g is expressed as:

$$g(T, \underline{\underline{\sigma}}, \underline{H}, z_0, z_1, z_2, z_3) = g_{therm} + g_{mec} + g_{mag} + g_{int} \quad (1)$$

with the thermal energy g_{therm} , the mechanical energy g_{mec} , the magnetic energy g_{mag} and the interaction energy g_{int} given below:

$$g_{therm}(T, z_0) = \lambda \left(T - T_0 - T \ln \left(\frac{T}{T_0} \right) \right) + z_0 (c_0 - c_1 T) \quad (2a)$$

$$g_{mec}(\underline{\underline{\sigma}}, z_0, z_1, z_2, z_3) = -\frac{1}{2}z_0\underline{\underline{\sigma}}:\underline{\underline{S}}_A:\underline{\underline{\sigma}} - \frac{1}{2}(1-z_0)\underline{\underline{\sigma}}:\underline{\underline{S}}_M:\underline{\underline{\sigma}} + z_1(\sigma_{xx}\varepsilon_c - (\sigma_{yy} + \sigma_{zz})\varepsilon_a) + z_2(\sigma_{yy}\varepsilon_c - (\sigma_{zz} + \sigma_{xx})\varepsilon_a) + z_3(\sigma_{zz}\varepsilon_c - (\sigma_{xx} + \sigma_{yy})\varepsilon_a) \quad (2b)$$

$$g_{mag}(\underline{H}, z_0, z_1, z_2, z_3) = -z_0\left(\frac{1}{2}\mu_0 a_0 |H|^2 + \langle |H| - \frac{M_s^A}{a_0} \rangle \left(\mu_0 M_s^A |H| - \frac{1}{2}\mu_0 a_0 |H|^2 - \frac{1}{2a_0}\mu_0 (M_s^A)^2\right)\right) - \sum_{i=1}^3 z_i \left(\frac{1}{2}\mu_0 a_i |H|^2 + \langle |H| - \frac{M_s^M}{a_i} \rangle \left(\mu_0 M_s^M |H| - \frac{1}{2}\mu_0 a_i |H|^2 - \frac{1}{2a_i}\mu_0 (M_s^M)^2\right)\right) \quad (2c)$$

$$g_{int}(z_0, z_1, z_2, z_3) = \frac{1}{2}k_0 z_0^2 + \frac{1}{2}k(z_1^2 + z_2^2 + z_3^2) \quad (2d)$$

where λ is the specific heat per unit volume, T_0 is a reference temperature (e.g. the temperature of the environment), c_0 is the internal energy difference between austenite and martensite at 0 K and c_1 is the entropy difference between austenite and martensite at 0 K; $\underline{\underline{S}}_A$ and $\underline{\underline{S}}_M$ are respectively the elastic compliance tensors of austenite and martensite, ε_a and ε_c are the strain changes respectively along the long and the short axis of the pseudo-tetragonal martensite during the martensitic phase transformation; μ_0 ($= 4\pi \times 10^{-7} \text{ T} \cdot \text{m} \cdot \text{A}^{-1}$) is the vacuum permeability, $|H|$ is the magnitude of the magnetic field strength, M_s^A and M_s^M are respectively the saturation magnetization of austenite and martensite, a_0 and a_i ($i = 1, 2, 3$) are respectively the magnetic susceptibility of austenite and martensite variant i , the function $\langle x \rangle$ is defined as: $\{0, \text{ if } x < 0; 1, \text{ if } x \geq 0\}$; k and k_0 are interaction parameters accounting for the incompatibility among martensite variants and between austenitic and martensitic phases.

It is noted that the magnetic susceptibility a_i ($i = 1, 2, 3$) of the martensite variants reflect the overall effects of the magnetic domain wall motions and the local magnetization rotations on the global magnetization process (Likhachev and Ullakko, 2000). The parameters a_i ($i = 1, 2, 3$) depend on the direction of the internal magnetic field and the magneto-crystalline anisotropy energy. The analytical expressions of a_i and the detailed deductions are provided in Appendix A.

It is also noted that compared with the strain (6% ~ 10%) from the magnetic-field-induced martensite reorientation, the magnetostrictive strain $\varepsilon_{striction} = 0.005\%$ (Heczko, 2005a) of MSMA is negligible. Moreover, from the energy point of view, the magnetostrictive energy ($= \frac{1}{2}E\varepsilon_{striction}^2 = 62.5 \text{ J/m}^3$, with E being the Young's modulus given in Table 1) is much smaller than the usual thermodynamic driving force for the martensite reorientation of MSMA, i.e. the magnetic energy difference between martensite variants, which is the magneto-

crystalline anisotropy energy $K_u \approx 1.65 \times 10^5 \text{ J/m}^3$ in (He et al., 2011, 2012; Heczko, 2005b). Therefore, magnetostriction is ignored in this paper.

The state equations can be obtained from Eqs. (1) and (2) as:

- Stress–strain relation

$$\begin{aligned} \underline{\underline{\varepsilon}}^* &= -\frac{\partial g}{\partial \underline{\underline{\sigma}}} \\ \rightarrow \underline{\underline{\varepsilon}} &= \underline{\underline{\varepsilon}}^* - \underline{\underline{\varepsilon}}^{*(0)}(T = T_0, \underline{\underline{\sigma}} = \underline{\underline{0}}, \underline{\underline{H}} = \underline{\underline{0}}, z_0^{(0)}, z_1^{(0)}, z_2^{(0)}, z_3^{(0)}) \\ &= \frac{1+\nu}{E} \underline{\underline{\sigma}} - \frac{\nu}{E} (\text{tr} \underline{\underline{\sigma}}) \underline{\underline{I}} + z_{12}(\varepsilon_0 \underline{\underline{e}}_x \otimes \underline{\underline{e}}_x - \varepsilon_0 \underline{\underline{e}}_y \otimes \underline{\underline{e}}_y) + z_{23}(\varepsilon_0 \underline{\underline{e}}_y \otimes \underline{\underline{e}}_y - \varepsilon_0 \underline{\underline{e}}_z \otimes \underline{\underline{e}}_z) \\ &\quad + z_{31}(\varepsilon_0 \underline{\underline{e}}_z \otimes \underline{\underline{e}}_z - \varepsilon_0 \underline{\underline{e}}_x \otimes \underline{\underline{e}}_x) + z_{01}(-\varepsilon_c \underline{\underline{e}}_x \otimes \underline{\underline{e}}_x + \varepsilon_a \underline{\underline{e}}_y \otimes \underline{\underline{e}}_y + \varepsilon_a \underline{\underline{e}}_z \otimes \underline{\underline{e}}_z) \\ &\quad + z_{02}(\varepsilon_a \underline{\underline{e}}_x \otimes \underline{\underline{e}}_x - \varepsilon_c \underline{\underline{e}}_y \otimes \underline{\underline{e}}_y + \varepsilon_a \underline{\underline{e}}_z \otimes \underline{\underline{e}}_z) + z_{03}(\varepsilon_a \underline{\underline{e}}_x \otimes \underline{\underline{e}}_x + \varepsilon_a \underline{\underline{e}}_y \otimes \underline{\underline{e}}_y - \varepsilon_c \underline{\underline{e}}_z \otimes \underline{\underline{e}}_z) \end{aligned} \quad (3)$$

where $\underline{\underline{\varepsilon}}$ is the strain change during the thermal-magneto-mechanical loadings, E and ν are respectively the Young's modulus and the Poisson's ratio of MSMA (assuming that the austenitic and martensitic phases are elastically isotropic with identical E and ν), $\text{tr} \underline{\underline{\sigma}}$ is the trace of the stress tensor, $\underline{\underline{I}}$ is the identity tensor, ε_0 is the strain change due to martensite reorientation, z_{12} , z_{23} , z_{31} , z_{01} , z_{02} and z_{03} denote the volume-fraction transformations between the martensite variants and between martensitic and austenitic phases, as shown in Fig. 1(b), $z_0^{(0)}$, $z_1^{(0)}$, $z_2^{(0)}$ and $z_3^{(0)}$ are the initial volume fractions of austenite and martensite variants. The current volume fractions z_0 , z_1 , z_2 and z_3 are related to the initial ones ($z_0^{(0)}$, $z_1^{(0)}$, $z_2^{(0)}$ and $z_3^{(0)}$) by:

$$z_0 = z_0^{(0)} - z_{01} - z_{02} - z_{03} \quad (4a)$$

$$z_1 = z_1^{(0)} - z_{12} + z_{31} + z_{01} \quad (4b)$$

$$z_2 = z_2^{(0)} - z_{23} + z_{12} + z_{02} \quad (4c)$$

$$z_3 = z_3^{(0)} - z_{31} + z_{23} + z_{03} \quad (4d)$$

- Magnetization–magnetic field relation

$$\begin{aligned} |M| &= -\frac{1}{\mu_0} \frac{\partial g}{\partial |H|} \\ \rightarrow |M| &= z_0 \left(a_0 |H| + \langle |H| - \frac{M_s^A}{a_0} \rangle (M_s^A - a_0 |H|) \right) + \sum_{i=1}^3 z_i \left(a_i |H| + \langle |H| - \frac{M_s^M}{a_i} \rangle (M_s^M - a_i |H|) \right) \end{aligned} \quad (5)$$

- Thermodynamic forces for martensite reorientation

The thermodynamic force $A_{i \leftrightarrow j}$ for the martensite reorientation between variant i ($= 1, 2, 3$) and j ($= 2, 3, 1$) is (Chen et al., 2014):

$$A_{i \leftrightarrow j} = \left(-\frac{\partial g}{\partial z_j} \right) - \left(-\frac{\partial g}{\partial z_i} \right) \rightarrow A_{ij} = k(z_i - z_j) + \varepsilon_0(\sigma_{ii} - \sigma_{jj}) + E_{i \leftrightarrow j}^H \quad (6)$$

where σ_{ii} and σ_{jj} are respectively the normal stress along the short axis of variant i and j , $E_{i \leftrightarrow j}^H$ is the magnetic energy difference between variant i and j , being:

$$E_{i \leftrightarrow j}^H = \frac{1}{2} \mu_0 a_j |H|^2 + \langle |H| - \frac{M_s^M}{a_j} \rangle \left(\mu_0 M_s^M |H| - \frac{1}{2} \mu_0 a_j |H|^2 - \frac{1}{2a_j} \mu_0 (M_s^M)^2 \right) - \frac{1}{2} \mu_0 a_i |H|^2 - \langle |H| - \frac{M_s^M}{a_i} \rangle \left(\mu_0 M_s^M |H| - \frac{1}{2} \mu_0 a_i |H|^2 - \frac{1}{2a_i} \mu_0 (M_s^M)^2 \right) \quad (7)$$

According to the model of martensite reorientation in (Chen et al., 2014), if the absolute value of the thermodynamic force $|A_{i \leftrightarrow j}|$ is smaller than $\sigma_{tw}^{eff} \varepsilon_0$, with σ_{tw}^{eff} being the effective twinning stress, there is no martensite reorientation between variant i and j . If $|A_{i \leftrightarrow j}| = \sigma_{tw}^{eff} \varepsilon_0$, martensite reorientation takes place, and z_i and z_j can be determined with the aid of Eqs. (4), (6) and the condition $|A_{i \leftrightarrow j}| = \sigma_{tw}^{eff} \varepsilon_0$.

This simple threshold-like evolution law can describe the martensite reorientation of MSMA not only in the quasi-static tests, but also in most of the normal dynamic tests (Pascan, 2015; Pascan et al., 2015; Zhang et al., 2018a) where numerous interfaces/twin boundaries are nucleated so that the propagation speed of individual interface is not high (i.e. less than 0.5 m/s). If an interface moves extremely fast as in the dynamic tests on a single twin boundary motion in (Faran et Shilo, 2011, 2012, 2013), the evolution law should include both the threshold and the rate-dependent parts.

Studies on the kinetics of single twin boundary motion have been reported in the literature (Faran et Shilo, 2011, 2012, 2013; Zreihan et al., 2018). However, the rate dependence of single twin boundary motion may not be simply applied to represent the rate sensitivity of the global (structural) twinning behaviour of a specimen at high loading rates because the simultaneous nucleation and propagation of numerous interfaces (twin boundaries) of different types and their interactions with the non-uniform coupling thermo-magneto-mechanical fields in the MSMA specimen must be considered. Further systematic experiments/modelling at macro-, meso- and micro-scales are needed to better understand the strain-rate dependence of the global (structural) twinning behaviour in MSMA under various loading rates, especially the very high loading rates like the impact tests in the traditional shape memory alloys (e.g. polycrystalline NiTi in (Nemat-Nasser et al., 2005)).

- Thermodynamic forces for phase transformation

The thermodynamic force A_{0i} for the phase transformation between austenite and martensite variant i ($= 1, 2, 3$) is (Gauthier, 2007):

$$A_{0i} = \left(-\frac{\partial g}{\partial z_i}\right) - \left(-\frac{\partial g}{\partial z_0}\right)$$

$$\rightarrow A_{0i} = (k_0 z_0 - k z_i) - \sigma_{ii} \varepsilon_c + \left(\text{tr} \underline{\underline{\sigma}} - \sigma_{ii}\right) \varepsilon_a + (c_0 - c_1 T) + E_{0i}^H \quad (8)$$

where the magnetic energy difference E_{0i}^H between austenite and martensite variant i is:

$$E_{0i}^H = \frac{1}{2} \mu_0 a_i |H|^2 + \langle |H| - \frac{M_s^M}{a_i} \rangle \left(\mu_0 M_s^M |H| - \frac{1}{2} \mu_0 a_i |H|^2 - \frac{1}{2 a_i} \mu_0 (M_s^M)^2 \right) -$$

$$\frac{1}{2} \mu_0 a_0 |H|^2 - \langle |H| - \frac{M_s^A}{a_0} \rangle \left(\mu_0 M_s^A |H| - \frac{1}{2} \mu_0 a_0 |H|^2 - \frac{1}{2 a_0} \mu_0 (M_s^A)^2 \right) \quad (9)$$

2.1.2. Evolution laws for phase transformation

An evolution law of phase transformation describes the relation between the volume-fraction transformation rate \dot{z}_{0i} ($i = 1, 2, 3$) and the corresponding thermodynamic force A_{0i} as shown in Fig 2. To demonstrate the significant role of the evolution law, two typical kinetics are adopted for a comparative study: the linear kinetics in Fig. 2(a) and the hysteretic kinetics in Fig. 2(b):

- Linear kinetics (Fig. 2(a))

The volume-fraction transformation rate \dot{z}_{0i} ($i = 1, 2, 3$) is proportional to the corresponding thermodynamic force A_{0i} : $\dot{z}_{0i} = L A_{0i}$, with L being a linear coefficient. This is one of the simplest evolution laws and it is widely adopted in the phase field models of MSMA (e.g. Jin, 2009; Li et al., 2011; Peng et al., 2015; Wu et al., 2011). As shown in Fig. 2(a), this linear evolution law is a viscosity-like kinetics without the friction-like hysteresis between the forward and reverse martensitic transformations.

- Hysteretic kinetics (Fig. 2(b))

This evolution law is normally used to account for the hysteresis of phase transformation. It is widely adopted in the models of the thermodynamic irreversible processes for the traditional shape memory alloys (e.g. Auricchio et al., 2014; Cisse et al., 2016; Lagoudas et al., 2006; LExcellent et al., 2000; Patoor et al., 2006; Zaki and Moumni, 2007). In the simplest form of this evolution law (i.e. similar to plasticity), it is supposed that the phase transformation can only take place when the thermodynamic force A_{0i} ($i = 1, 2, 3$) reaches

a threshold D_p (related to some internal frictional force). Then the pseudo-dissipation potential D of the phase transformation can be assumed as:

$$D = D_p \sum_{i=1}^3 |\dot{z}_{0i}| \quad (10)$$

The directional derivatives of D define the yield surface for the thermodynamic forces A_{0i} .

Using Eq. (10), we obtain:

$$A_{0i} \in \partial_{\dot{z}_{0i}} D \rightarrow |A_{0i}| \leq D_p \quad (11)$$

From Eq. (11), we derive the following evolution law for the transformation rate \dot{z}_{0i} :

- If $|A_{0i}| < D_p$, there is no phase transformation between austenite (A) and martensite variant i (M_i), so $\dot{z}_{0i} = 0$.
- If $|A_{0i}| = D_p$ and $\dot{A}_{0i} \frac{A_{0i}}{|A_{0i}|} < 0$, there is no phase transformation between A and M_i , then $\dot{z}_{0i} = 0$.
- If $|A_{0i}| = D_p$ and $\dot{A}_{0i} = 0$, phase transformation between A and M_i takes place. With the aid of Eqs. (4) and (8), we obtain: $\dot{A}_{0i} = 0 \rightarrow \dot{z}_{0i} = \frac{1}{(k_0+k)} \left(-\dot{\sigma}_{ii} \varepsilon_c + \left(tr \underline{\underline{\dot{\sigma}}} - \dot{\sigma}_{ii} \right) \varepsilon_a - c_1 \dot{T} + \dot{E}_{0i}^H \right)$.

2.1.3. Identification of model parameters

The model parameters E , k , ε_0 , M_S^M and a_i ($i = 1, 2, 3$) can be determined by a uniaxial compression test and two magnetization tests detailed in (Chen et al., 2014). Moreover, a magnetization test on austenite can determine a_0 and M_S^A , and an X-ray diffraction test can determine ε_a and ε_c . The Poisson's ratio ν can be assumed to be 0.33 since ν of the conventional engineering metals and alloys is around 1/3.

Experiments in the literature (Sozinov et al., 2011; Straka et al., 2010, 2011) show that two types of twins can participate in the martensite reorientation of MSMA. They are: Type I twin whose twinning plane is rational, and Type II twin whose shearing direction is rational (Bhattacharya, 2003). Our high-frequency dynamic tests (Pascan et al., 2015; Zhang et al., 2018a) further demonstrate that both the two types (I and II) can be nucleated in the dynamic loadings and their fractions depend on the material's response frequency, i.e. Type I twin is dominant in low frequencies, while in high frequencies, Type II twin is dominant. The origin and the microscopic mechanism for such frequency effect on the nucleation of Type I and II twins are still unclear. To estimate the effective twinning stress σ_{tw}^{eff} , we take the average twinning stresses of Type I and II twins according to the material's response frequency. The

twinning stresses of these two types of twins have different temperature dependences: the twinning stress of Type I twin increases linearly with decreasing temperature, while that of Type II is temperature independent (Straka et al., 2012). Based on our experiments and the previous experiments in the literature, we propose the following expression to estimate σ_{tw}^{eff} , considering both the frequency effect on the fraction of twins and the temperature dependence (Zhang et al., 2018a):

$$\sigma_{tw}^{eff}(T, f_{strain}) = 0.2 - 0.04 \times (T - A_s^0) \times v(f_{strain}) \quad [\text{MPa}] \quad (12)$$

where f_{strain} is the frequency of the output strain (i.e. mechanical response of the material), A_s^0 is the austenite start temperature in the free state (without mechanical stress or magnetic field), and v is the contribution fraction of Type I twin. The measured values of v at different levels of f_{strain} in (Zhang et al., 2018a) are summarized in Fig. 3, from which an approximation function is proposed for the experiments in (Zhang et al., 2018a):

$$v(f_{strain}) = \frac{1}{2} \left(1 - \tanh \frac{f_{strain} - 199}{85} \right) \quad (13)$$

Introducing Eq. (13) into Eq. (12), we finally obtain:

$$\sigma_{tw}^{eff} = 0.2 - 0.02 \times (T - A_s^0) \times \left(1 - \tanh \frac{f_{strain} - 199}{85} \right) \quad (14)$$

A DSC (Differential Scanning Calorimetry) test corresponding to the hysteretic phase transformation in the quasi-static loading condition can determine the model parameters λ , c_0 , c_1 , k_0 and D_p . The test directly measures the specific heat per unit volume λ and the phase transformation temperatures M_s^0 , M_f^0 , A_s^0 and A_f^0 , which correspond respectively to the martensite start and finish temperatures, and the austenite start and finish temperatures in the free state (without mechanical stress or magnetic field). According to the evolution law for the hysteretic phase transformation in Subsection 2.1.2, during the forward martensitic transformation (z_1 , z_2 and z_3 are increasing), the corresponding thermodynamic forces A_{01} , A_{02} and A_{03} must be equal to D_p . At the start of the transformation, $z_0 = 1$, $z_1 = z_2 = z_3 = 0$, and $T = M_s^0$. Then using Eq. (8), we have:

$$A_{01} = A_{02} = A_{03} = D_p \rightarrow k_0 + c_0 - c_1 M_s^0 = D_p \quad (15a)$$

At the end of the transformation, $T = M_f^0$, $z_0 = 0$, $z_1 = z_2 = z_3 = 1/3$ (assuming that the martensite variants have the same volume fraction in the free state, i.e. without mechanical stress or magnetic field). Then we have:

$$A_{01} = A_{02} = A_{03} = D_p \rightarrow -\frac{1}{3}k + c_0 - c_1 M_f^0 = D_p \quad (15b)$$

Similarly, for the reverse martensitic transformation we have:

$$A_{01} = A_{02} = A_{03} = -D_p \Rightarrow -\frac{1}{3}k + c_0 - c_1 A_s^0 = -D_p \quad (16a)$$

$$k_0 + c_0 - c_1 A_f^0 = -D_p \quad (16b)$$

By solving Eqs. (15) and (16), we obtain:

$$D_p = \frac{1}{2}(A_f^0 - M_s^0)c_1 = \frac{1}{2}(A_s^0 - M_f^0)c_1 \quad (17a)$$

$$c_0 = \frac{1}{3}k + \frac{1}{2}(A_s^0 + M_f^0)c_1 \quad (17b)$$

$$k_0 = -\frac{1}{3}k + (A_f^0 - A_s^0)c_1 = -\frac{1}{3}k + (M_s^0 - M_f^0)c_1 \quad (17c)$$

The same parameter k_0 is used in the model to account for the incompatibility during both forward and reverse martensitic transformations. This implies that: $M_s^0 - M_f^0 = A_f^0 - A_s^0$. Experiments in the literature also confirm that the difference between the martensite start and finish temperatures is close to that between the austenite start and finish temperatures, e.g. $M_s^0 - M_f^0 = 40$ K and $A_f^0 - A_s^0 = 45$ K in (Karaca et al., 2006), $M_s^0 - M_f^0 = 1$ K and $A_f^0 - A_s^0 = 0.7$ K in (Zhang et al., 2018a).

The DSC test also measures the released (H_l^1) and the absorbed (H_l^2) latent heat during the phase transformations. From Eqs. (1) and (2), we can calculate the latent heat H_l as:

$$H_l = \int T \frac{\partial^2 g}{\partial T \partial z_0} dz_0 \rightarrow H_l = -c_1 \int T dz_0 \quad (18)$$

For the forward martensitic transformation, z_0 changes from 1 to 0, and T changes from M_s^0 to M_f^0 . By taking $T = \frac{1}{2}(M_s^0 + M_f^0)$ in Eq. (18), we estimate the released latent heat H_l^1 (positive) for the forward martensitic transformation as:

$$H_l^1 = -\frac{1}{2}c_1(M_s^0 + M_f^0) \int_1^0 dz_0 \rightarrow H_l^1 = \frac{1}{2}c_1(M_s^0 + M_f^0)$$

from which the parameter c_1 is obtained as:

$$c_1 = \frac{2H_l^1}{M_s^0 + M_f^0} \quad (19a)$$

Similarly, for the reverse martensitic transformation, we have:

$$c_1 = -\frac{2H_l^2}{A_s^0 + A_f^0} \quad (19b)$$

where H_l^2 is the absorbed latent heat (negative) during the reverse transformation. Theoretically, the values of c_1 obtained from Eqs. (19a) and (19b) are identical. By introducing the value of c_1 into Eq. (17), the values of D_p , c_0 and k_0 can be determined.

2.2. Mass-spring model of the MSMA dynamic system

In order to take into account the inertial effect, we develop a mass-spring model to describe the dynamic behaviours of MSMA system in (Zhang et al., 2018a). The constitutive model in Subsection 2.1 is embedded in the mass-spring model. The modelling and the simulation include the magnetic analysis, the mechanical analysis and the thermal analysis, which are described in details below.

2.2.1. Magnetic analysis

The experimental setup in (Zhang et al., 2018a) is shown in Fig. 4(a): The MSMA sample is supported at the bottom end by a sample holder and compressed at the top end by a spring along x -axis. At the same time, a magnetic field is applied by an electromagnet along a fixed direction, i.e. y -axis in Fig. 4(a). So the y -component of the magnetic field strength vector is the main component. For simplicity, we only consider the y -component of the magnetic field here. Due to the demagnetization effect, the magnetic field inside the MSMA sample, so-called the internal magnetic field H (y -component), is smaller than the applied one H^{app} . H can be estimated as:

$$H = H^{app} - NM \quad (20)$$

where N is the demagnetization factor, whose value is given in Table 1 by using the formula for the volume average demagnetization factors of rectangular prisms in (Aharoni, 1998); M is the magnetization of the material, being:

$$M = z_0 M_0 + z_1 M_1 + z_2 M_2 + z_3 M_3 \quad (21)$$

where M_0 , M_1 , M_2 and M_3 are respectively the magnetization of austenite, martensite variant 1, 2 and 3 (denoted by A, M1, M2 and M3 in Fig. 1(a)).

Before each test in (Zhang et al., 2018a), a large compressive stress along x -axis is applied on the MSMA sample so that the sample is in the initial state of single martensite variant, i.e. M1 in Fig. 1(a). Therefore, the initial volume fraction $z_1^{(0)}$ of M1 is set to be 1 in the model, as shown in Table 1. To simulate the loading condition in Fig. 4(a), the compressive spring force along x -axis and the magnetic field along y -axis are considered in the model. M1 is energetically favoured by the compressive force along x -axis (i.e. M1 has the lowest mechanical energy calculated from Eq. 2(b)) and M2 (see Fig. 1(a)) is energetically favoured by the magnetic field along y -axis (i.e. M2 has the lowest magnetic energy calculated by Eq. 2(c)). But the third martensite variant, i.e. M3 in Fig. 1(a), is neither energetically favoured by the compressive stress along x -axis (largest mechanical energy calculated from Eq. (2b)) nor

the magnetic field along y-axis (largest magnetic energy calculated from Eq. (2c)). As a result, the thermodynamic forces $A_{2\leftrightarrow 3}$ and $A_{3\leftrightarrow 1}$ given in Eq. (6) never reach the effective twinning stress in the simulation and the associated martensite reorientation from M1 and M2 to M3 is never triggered, which agrees with the detailed analysis of the material under 3D magneto-mechanical loading conditions in (He et al., 2012). So the volume fraction z_3 of M3 is always 0 and Eq. (21) can be reduced to:

$$M = z_0M_0 + z_1M_1 + z_2M_2 \quad (22)$$

From the magnetization–magnetic field relation (Eq. (5)), we can obtain the absolute value $|M_0|$ by taking $z_0 = 1$ and $z_i = 0$, $|M_i|$ ($i = 1, 2$) by taking $z_0 = 0$ and $z_i = 1$. The sign of the internal magnetic field H is further introduced as: positive H along y-axis and negative H along the opposite direction of y-axis. Then the values of M_0 and M_i ($i = 1, 2$) can be obtained from their absolute values as:

$$M_0 = \begin{cases} -M_s^A & \left(H \leq -\frac{M_s^A}{a_0}\right) \\ a_0H & \left(-\frac{M_s^A}{a_0} < H < \frac{M_s^A}{a_0}\right) \\ M_s^A & \left(H \geq \frac{M_s^A}{a_0}\right) \end{cases} \quad (23a)$$

$$M_i = \begin{cases} -M_s^M & \left(H \leq -\frac{M_s^M}{a_i}\right) \\ a_iH & \left(-\frac{M_s^M}{a_i} < H < \frac{M_s^M}{a_i}\right) \\ M_s^M & \left(H \geq \frac{M_s^M}{a_i}\right) \end{cases} \quad (i = 1, 2) \quad (23b)$$

2.2.2. Mechanical analysis

Figure 4(a) shows the experimental setup in (Zhang et al., 2018a). When the cyclic magnetic field is applied, cyclic martensite reorientation between variant 1 and 2 is triggered (see the inset of Fig. 4(b)). The MSMA sample and the upper sample holder (moving parts in the experiment) are treated as a lumped mass, and the corresponding dynamic system is shown in Fig. 4(b).

The MSMA sample is in the initial state of martensite variant 1 (M1 in the inset of Fig. 4(b)). An initial compressive stress σ_0 is applied on the sample by a spring with stiffness k_s . So the spring is compressed by an initial distance Δx_1 and the mass in Fig. 4(b) has an initial displacement Δx_2 , being:

$$\Delta x_1 = \frac{\sigma_0 S}{k_s} \quad (24a)$$

$$\Delta x_2 = -\frac{\sigma_0}{E} l_0 \quad (24b)$$

where S and l_0 are respectively the cross-sectional area and the initial length of the MSMA sample. The 1D equilibrium equation of the mass-spring model in Fig. 4(b) is:

$$m\ddot{x} + c\dot{x} + f_{spring} + f_{MSMA} = 0 \quad (25)$$

where m is the total mass of the dynamic system including the MSMA sample and the upper sample holder, x is the displacement of the mass with respect to its initial displacement, c is a damping coefficient, f_{spring} is the spring force and f_{MSMA} is the restoring force provided by the MSMA sample itself. The values of m and c are given in Table 1. f_{spring} can be calculated as:

$$f_{spring} = k_s(x + \Delta x_1) \quad (26)$$

where Δx_1 is the initial length change of the spring given in Eq. (24a).

Using the stress-strain relation given in Eq. (3) and only considering the components along x -axis, we obtain:

$$\varepsilon_{xx} = \frac{\sigma_{xx}}{E} + z_{12}\varepsilon_0 - z_{01}\varepsilon_c + z_{02}\varepsilon_a \quad (27)$$

The strain change ε_{xx} can also be calculated as:

$$\varepsilon_{xx} = \frac{x + \Delta x_2}{l_0} \quad (28)$$

where Δx_2 is the initial displacement of the mass given in Eq. (24b). Introducing Eq. (28) into Eq. (27) and after several calculations we obtain:

$$f_{MSMA} = S\sigma_{xx} \rightarrow f_{MSMA} = ES \left(\frac{x + \Delta x_2}{l_0} - z_{12}\varepsilon_0 + z_{01}\varepsilon_c - z_{02}\varepsilon_a \right) \quad (29)$$

Introducing Eqs. (24), (26) and (29) into Eq. (25), we obtain the equilibrium equation for the mechanical analysis as:

$$m\ddot{x} + c\dot{x} + \left(k_s + E \frac{S}{l_0} \right) x = ES(z_{12}(H) \cdot \varepsilon_0 - z_{01}\varepsilon_c + z_{02}\varepsilon_a) \quad (30)$$

When the internal magnetic field strength H reaches certain level, the martensite reorientation between M1 and M2 is triggered and the volume-fraction transformation z_{12} varies with H . So z_{12} is expressed as a function of H in Eq. (30). On the other hand, to trigger the phase transformation of MSMA, a large magnetic field (> 5 T) is required (Haldar et al., 2014; Karaca et al., 2009) since the saturation magnetization difference between austenite and martensite is small. In the experiments of (Zhang et al., 2018a), only a small magnetic field (< 1 T) is applied. So the applied magnetic field cannot trigger the phase transformation and the effect of the magnetic field strength H on z_{01} and z_{02} is ignored in Eq. (30) for simplicity.

To detect the martensite reorientation and determine the expression of z_{12} , we first use Eq. (6) to calculate the thermodynamic force $A_{1 \leftrightarrow 2}$ for the martensite reorientation between M1 and M2 as:

$$A_{1\leftrightarrow 2} = k(z_1 - z_2) + \varepsilon_0 \sigma_{xx} + E_{1\leftrightarrow 2}^H \quad (31)$$

where the volume fractions z_1 and z_2 , the stress σ_{xx} of the MSMA sample, and the magnetic energy difference $E_{1\leftrightarrow 2}^H$ can be obtained from Eqs. (4), (7), (24) and (29) as:

$$z_1 = z_1^{(0)} - z_{12} + z_{01} \quad (32a)$$

$$z_2 = z_2^{(0)} + z_{12} + z_{02} \quad (32b)$$

$$\sigma_{xx} = \frac{f_{FSMA}}{s} = E \left(\frac{x}{l_0} - z_{12} \varepsilon_0 + z_{01} \varepsilon_c - z_{02} \varepsilon_a \right) - \sigma_0 \quad (32c)$$

$$E_{1\leftrightarrow 2}^H = \frac{1}{2} \mu_0 a_2 |H|^2 + \langle |H| - \frac{M_s^M}{a_2} \rangle \left(\mu_0 M_s^M |H| - \frac{1}{2} \mu_0 a_2 |H|^2 - \frac{1}{2a_2} \mu_0 (M_s^M)^2 \right) - \frac{1}{2} \mu_0 a_1 |H|^2 - \langle |H| - \frac{M_s^M}{a_1} \rangle \left(\mu_0 M_s^M |H| - \frac{1}{2} \mu_0 a_1 |H|^2 - \frac{1}{2a_1} \mu_0 (M_s^M)^2 \right) \quad (32d)$$

Introducing Eq. (32) into Eq. (31), we obtain:

$$A_{1\leftrightarrow 2} = \frac{E \varepsilon_0}{l_0} x + k \left(z_1^{(0)} - z_2^{(0)} + z_{01} - z_{02} \right) - \sigma_0 \varepsilon_0 + E_{1\leftrightarrow 2}^H + E \varepsilon_0 (z_{01} \varepsilon_c - z_{02} \varepsilon_a) - z_{12} (2k + E \varepsilon_0^2) \quad (33)$$

According to the constitutive model in Subsection 2.1, we have following three cases to consider:

- When $|A_{1\leftrightarrow 2}| < \sigma_{tw}^{eff} \varepsilon_0$, with σ_{tw}^{eff} being given in Eq. (14), there is no martensite reorientation. So z_{12} does not vary with H and Eq. (30) can be reduced to:

$$m\ddot{x} + c\dot{x} + \left(k_s + E \frac{S}{l_0} \right) x = ES (z_{12} \varepsilon_0 - z_{01} \varepsilon_c + z_{02} \varepsilon_a) \quad (34)$$

- When $A_{1\leftrightarrow 2} = \sigma_{tw}^{eff} \varepsilon_0$, M1 switches to M2. Then we can obtain z_{12} from Eq. (33) as:

$$A_{1\leftrightarrow 2} = \sigma_{tw}^{eff} \varepsilon_0 \rightarrow z_{12}(H) = \frac{1}{2k + E \varepsilon_0^2} \left(\frac{E \varepsilon_0}{l_0} x + k \left(z_1^{(0)} - z_2^{(0)} + z_{01} - z_{02} \right) - \sigma_0 \varepsilon_0 + E_{1\leftrightarrow 2}^H + E \varepsilon_0 (z_{01} \varepsilon_c - z_{02} \varepsilon_a) - \sigma_{tw}^{eff} \varepsilon_0 \right) \quad (35a)$$

Introducing Eq. (35a) into Eq. (30), we have:

$$m\ddot{x} + c\dot{x} + \left(k_s + \frac{2k}{\varepsilon_0^2} \frac{E}{E + \frac{2k}{\varepsilon_0^2}} \frac{S}{l_0} \right) x = \frac{ES \varepsilon_0}{2k + E \varepsilon_0^2} \left(k \left(z_1^{(0)} - z_2^{(0)} + z_{01} - z_{02} \right) - \sigma_0 \varepsilon_0 + E_{1\leftrightarrow 2}^H - \sigma_{tw}^{eff} \varepsilon_0 \right) - \frac{2kES}{2k + E \varepsilon_0^2} (z_{01} \varepsilon_c - z_{02} \varepsilon_a) \quad (35b)$$

- When $A_{1\leftrightarrow 2} = -\sigma_{tw}^{eff} \varepsilon_0$, M2 switches to M1. Following similar procedures, we obtain:

$$z_{12}(H) = \frac{1}{2k + E \varepsilon_0^2} \left(\frac{E \varepsilon_0}{l_0} x + k \left(z_1^{(0)} - z_2^{(0)} + z_{01} - z_{02} \right) - \sigma_0 \varepsilon_0 + E_{1\leftrightarrow 2}^H + E \varepsilon_0 (z_{01} \varepsilon_c - z_{02} \varepsilon_a) + \sigma_{tw}^{eff} \varepsilon_0 \right) \quad (36a)$$

$$m\ddot{x} + c\dot{x} + \left(k_s + \frac{2k}{\varepsilon_0^2} \frac{E}{\left(E + \frac{2k}{\varepsilon_0^2} \right) l_0} \frac{S}{\varepsilon_0} \right) x = \frac{ES\varepsilon_0}{2k+E\varepsilon_0^2} \left(k \left(z_1^{(0)} - z_2^{(0)} + z_{01} - z_{02} \right) - \sigma_0 \varepsilon_0 + E_{1 \leftrightarrow 2}^H + \sigma_{tw}^{eff} \varepsilon_0 \right) - \frac{2kES}{2k+E\varepsilon_0^2} (z_{01} \varepsilon_c - z_{02} \varepsilon_a) \quad (36b)$$

2.2.3. Thermal analysis

The temperature evolution due to heat generation and heat convection can be estimated by the following 1D heat equation (He and Sun, 2010a, 2011; Pascan et al., 2015):

$$\lambda \dot{T} = r_{tot} - \frac{2h}{R} (T - T_0) \quad (37)$$

where $R (= \frac{ab}{a+b})$, with a and b being respectively the width and thickness of the MSMA sample) is the effective radius of the MSMA sample; h is the heat convection coefficient, which is related to a characteristic ambient heat-transfer time t_h by: $h = \frac{\lambda R}{2t_h}$; T_0 is the temperature of the environment; r_{tot} is the total heat generation rate, being:

$$r_{tot} = r_{eddy} + r_{MR} + r_{PT} \quad (38)$$

where r_{eddy} , r_{MR} and r_{PT} are respectively the heat generation rate due to the eddy current power loss, the intrinsic dissipation of martensite reorientation, and the phase transformation:

$$r_{eddy} = 2320.7 f_{strain} - 1.35 \times 10^5 \quad (39a)$$

$$r_{MR} = \sigma_{tw}^{eff} \varepsilon_0 |\dot{z}_{12}| \quad (39b)$$

$$r_{PT} = A_{01} \dot{z}_{01} + A_{02} \dot{z}_{02} + c_1 T (\dot{z}_{01} + \dot{z}_{02}) \quad (39c)$$

Equation (39a) is proposed in (Zhang et al., 2018a) for the experiments in the strain frequency range of 100 Hz ~ 400 Hz. The sum of the first two terms on the right-hand side of Eq. (39c) is the intrinsic dissipation of phase transformation, and the third term is the latent heat obtained from Eqs. (4a) and (18). Introducing Eqs. (38) and (39) into Eq. (37), we obtain the following equation to calculate the temperature evolution:

$$\lambda \dot{T} = (2320.7 f_{strain} - 1.35 \times 10^5) + \sigma_{tw}^{eff} \varepsilon_0 |\dot{z}_{12}| + (A_{01} \dot{z}_{01} + A_{02} \dot{z}_{02} + c_1 T (\dot{z}_{01} + \dot{z}_{02})) - \frac{2h}{R} (T - T_0) \quad (40)$$

The thermodynamic forces A_{01} and A_{02} in Eq. (40) for the phase transformation can be calculated by only considering the x -components in Eq. (8):

$$A_{01} = (k_0 z_0 - k z_1) - \sigma_{xx} \varepsilon_c + (c_0 - c_1 T) + E_{01}^H \quad (41a)$$

$$A_{02} = (k_0 z_0 - k z_2) + \sigma_{xx} \varepsilon_a + (c_0 - c_1 T) + E_{02}^H \quad (41b)$$

where z_1 and z_2 are given in Eqs. (32a) and (32b), z_0 is obtained from Eq. (4a) as:

$$z_0 = z_0^{(0)} - z_{01} - z_{02} \quad (42)$$

Introducing Eqs. (32) and (42) into Eq. (41), we have:

$$A_{01} = -\frac{E\varepsilon_c}{l_0}x - (k_0 + k + E\varepsilon_c^2)z_{01} - (k_0 - E\varepsilon_a\varepsilon_c)z_{02} + k_0z_0^{(0)} - k(z_1^{(0)} - z_{12}) + E\varepsilon_0\varepsilon_c z_{12} + \sigma_0\varepsilon_c + (c_0 - c_1T) + E_{01}^H \quad (43a)$$

$$A_{02} = \frac{E\varepsilon_a}{l_0}x - (k_0 - E\varepsilon_a\varepsilon_c)z_{01} - (k_0 + k + E\varepsilon_a^2)z_{02} + k_0z_0^{(0)} - k(z_2^{(0)} + z_{12}) - E\varepsilon_0\varepsilon_a z_{12} - \sigma_0\varepsilon_a + (c_0 - c_1T) + E_{02}^H \quad (43b)$$

Depending on the evolution laws proposed in Subsection 2.1.2, we have following two different procedures to conduct the thermal analysis:

- Linear kinetics

With A_{01} and A_{02} calculated by Eq. (43), we further calculate: $\dot{z}_{01} = LA_{01}$ and $\dot{z}_{02} = LA_{02}$. Introducing the obtained values of \dot{z}_{01} and \dot{z}_{02} into Eq. (40), we can calculate the temperature evolution.

- Hysteretic kinetics

- If the calculated thermodynamic force A_{0i} ($i = 1, 2$) satisfies $|A_{0i}| < D_p$, take $\dot{z}_{0i} = 0$ in Eq. (40) to obtain the corresponding heat equation.

- If the calculated A_{0i} ($i = 1, 2$) satisfies $|A_{0i}| = D_p$, we obtain from Eq. (43) as: $\dot{A}_{0i} = 0 \rightarrow \dot{z}_{01} = \frac{1}{(k_0+k+E\varepsilon_c^2)} \left(-\frac{E\varepsilon_c}{l_0}\dot{x} + (k + E\varepsilon_0\varepsilon_c)\dot{z}_{12} - c_1\dot{T} + \dot{E}_{01}^H \right)$ for $i = 1$, and $\dot{z}_{02} = \frac{1}{(k_0+k+E\varepsilon_a^2)} \left(\frac{E\varepsilon_a}{l_0}\dot{x} - (k + E\varepsilon_0\varepsilon_a)\dot{z}_{12} - c_1\dot{T} + \dot{E}_{02}^H \right)$ for $i = 2$. Introducing the calculated \dot{z}_{01} and \dot{z}_{02} into Eq. (40), we can calculate the temperature evolution.

2.3. Program flowchart and values of model parameters

The dynamic model developed in Subsection 2.1 and 2.2 is used to simulate the experiments in (Zhang et al., 2018a), where a cyclic triangular magnetic field of fixed amplitude $\mu_0 H_{amp}^{app}$ is applied. Model simulations are conducted using the parameter values in Table 1 and the commercial software MATLAB. Every magnetic loading-unloading cycle is equally divided into 1000 time steps, and the flowchart of each time step is shown in Fig. 5. Since different evolution laws of phase transformation have different procedures of thermal analysis (see Subsection 2.2.3), two flowcharts corresponding to the two evolution laws proposed in Subsection 2.1.2 are shown. In each flowchart, there are two loops, i.e. an inner loop (indicated by a dotted rectangle) and an outer loop (enclosed by dashed lines):

- The inner loop is for the coupled martensite reorientation and phase transformation processes: if there is phase transformation, the temperature rate will change with the transformation rate (see Eq. (40)), which in return depends on the temperature, as shown by Eq. (43) for the thermodynamic forces of phase transformation. Moreover, the change of volume-fraction transformations (z_{01} , z_{02}) will affect martensite reorientation (see Eq. (33) for the thermodynamic force of matensite reorientation), which can change the temperature through Eq. (40).
- The outer loop is for the coupled thermo-magneto-mechanical analysis: the internal magnetic field H varies with the volume fractions z_1 and z_2 (Eqs. (20), (22) and (23)), which are determined by the martensite reorientation process. Conversely, H also has an effect on this process (Eqs. (33)).

It is noted that a constant demagnetization factor is used in the developed mass-spring model, as shown by Eq. (20) in Subsection 2.2.1. As most of the MSMA samples like that in (Zhang et al., 2018a) are rectangular, the magnetic field inside a rectangular sample is not homogeneous and a constant demagnetization factor cannot describe the accurate magnetic field distribution inside the sample. However, the inhomogeneous distributions of magnetic field are only around the corners of the sample, while most part (including the centre) of the sample has a nearly uniform distribution of magnetic field. Therefore, a constant demagnetization factor is valid to estimate the global effect of the magnetic field on the sample.

It is also noted that the developed mass-spring model only accounts for the spring force. During the high-frequency magnetic loading, the magnetic body forces and surface traction may also be significant (Haldar et al., 2011; Haldar and Lagoudas, 2018). However, for the experiments in (Zhang et al., 2018a), a small magnetic field (< 1 T) is applied and the field frequency is not large (≤ 200 Hz). Moreover, the field is applied in a narrow gap (5 mm) and along a fixed direction, i.e. the 2-mm edge of the MSMA sample. In this case, the magnetic body forces and surface traction are not significant with respect to the spring force applied during the experiments. Therefore, the developed mass-spring model only considering the spring force can capture the characteristics of the dynamic behaviours observed in (Zhang et al., 2018a).

3. Simulation results

The simulation result based on the flowchart of Fig. 5(a) with the linear phase transformation kinetics (Fig. 2(a)) is not the same as that based on the flowchart of Fig. 5(b)

with the hysteretic phase transformation kinetics (Fig. 2(b)). Interestingly, the simulation with the simple linear kinetics is better in capturing the dynamic phenomena. Therefore, the simulation with the linear kinetics is reported in this section and that with the hysteretic kinetics is discussed for comparison in Section 4.

3.1. Mass-spring harmonic oscillator of field-induced deformation

A typical example of the simulation results is shown in Fig. 6(a) where the applied magnetic field cyclically changes between -0.78 Tesla and $+0.78$ Tesla with the frequency $f_{magnetic} = 90$ Hz (so, the output strain frequency $f_{strain} = 2 \times f_{magnetic} = 180$ Hz), the initial compressive stress $\sigma_0 = 0.4$ MPa, the characteristic ambient heat-transfer time $t_h = 68.9$ seconds and the initial temperature $T_0 = 20$ °C. It is seen that, while the cyclic magnetic field is applied, the output strain oscillation amplitude $\Delta\epsilon$ first increases and then decreases to a steady-state value (0.6%) and the specimen temperature T increases to a saturated value (39.2 °C). For a clear demonstration, the magnified views on the response curves at several representative times ($t_1 \sim t_4$) are also shown in Fig. 6(a). At the beginning (see time t_1), the strain oscillation amplitude $\Delta\epsilon = 2.9\%$ and the volume fractions of the two martensite variants M1 and M2 (i.e., z_1 and z_2) have the oscillation amplitude of 0.50 while the volume fraction of the austenite (z_0) is kept at 0. That means, such deformation oscillation is due to the field-induced Martensite Reorientation (MR) between the variants M1 and M2. Continuing the magnetic actuation leads to the increases in both $\Delta\epsilon$ and T as shown in the magnified view at time t_2 where $\Delta\epsilon = 5.9\%$ and the volume fractions z_1 and z_2 vary between 0 and 1, implying a complete MR in the material. Such large dissipative deformation can result in a significant temperature rise. When the temperature T increases to a critical level triggering the Martensite-to-Austenite (M→A) phase transformation (e.g., z_0 increases to 0.55 while the variation amplitudes of z_1 and z_2 decrease to 0.45 as shown by the magnified view at t_3), the output strain amplitude $\Delta\epsilon$ decreases (i.e., from 5.9% at time t_2 to 2.7% at time t_3). That means, the reduction in strain amplitude $\Delta\epsilon$ is due to the decrease in the volume fractions of the martensite variants and the austenite phase (A phase) under this cyclic magnetic field contributes little to $\Delta\epsilon$, which agrees with the in-situ microstructural observations in (Zhang et al., 2018a). The increase in z_0 (i.e. increasing A phase) reduces not only $\Delta\epsilon$, but also the temperature rising rate, as shown by the magnified views of temperature at t_2 and t_3 . Finally, a steady state cyclic oscillation is obtained: T reaches a constant value of 39.2 °C and $\Delta\epsilon$ reduces to a much smaller level of 0.6% (see the magnified view at time t_4 where $z_0 = 0.91$ implying that the A phase is dominant and only a little martensite phase

remains). In other words, the appearance of A phase due to the temperature rise reduces the field-induced deformation significantly. This simulated strain drop (significant reduction in $\Delta\varepsilon$) agrees with the experimental observation under the same loading condition in Fig. 6(b). This strain-drop phenomenon also exists in other loading conditions, for example, at different frequencies in Fig. 7.

Figure 7 shows the dynamic evolutions of the magnetic-field-induced deformation at the output strain frequency $f_{strain} = 130$ Hz, 160 Hz, 200 Hz and 220 Hz, whose strain amplitudes all decrease to a small level due to the appearance of A phase when the temperature increases to a critical level around 39 °C. The maximum strain amplitude before the strain drop (i.e., before M→A phase transformation) is denoted by $\Delta\varepsilon_{unstable}$, which significantly depends on the frequency f_{strain} (e.g. $\Delta\varepsilon_{unstable}$ varies from 5.6% to 2.5% in Fig. 7). By contrast, the steady-state strain amplitude (denoted by $\Delta\varepsilon_{stable}$) and the steady-state temperature (T_{stable}) hardly depend on f_{strain} (e.g. $\Delta\varepsilon_{stable} = 0.5\% \sim 0.7\%$ and $T_{stable} = 39.2$ °C in Fig. 7). The frequency-dependence of $\Delta\varepsilon_{unstable}$ and the frequency-independence of $\Delta\varepsilon_{stable}$ can be clearly demonstrated by summarising all the simulation data and experimental observations in Fig. 8. It is seen that the strain amplitude $\Delta\varepsilon_{unstable}$ significantly depends on f_{strain} with a resonance at around 180 Hz. That means the field-induced cyclic martensite reorientation in the material demonstrates the dynamics with the mass-spring effect (a harmonic oscillator). By contrast, the steady-state strain amplitude $\Delta\varepsilon_{stable}$ (after M→A phase transformation introducing the coexistence of the A phase and the martensite variants) has little dependence on f_{strain} (without the obvious resonance frequency) and only takes very small values ($< 1\%$ in Fig. 8). It seems that the coupling of Martensite Reorientation (MR) and Phase Transformation (PT) introduces a large damping into the harmonic oscillator to weaken the resonance effect and reduce the oscillation.

To keep the advantage of the large deformation oscillation in the material for engineering applications, a method has been proposed to avoid the temperature-induced PT during the dissipative MR: increasing (enhancing) the heat exchange between the material and the ambient (e.g. by controlling the ambient airflow) to reduce the temperature rise (Zhang et al. 2018a). Interestingly, the controlled temperature variation not only influences PT, but also changes the effective twinning stress σ_{tw}^{eff} of MR (i.e. the temperature-dependent dissipation rate of MR in Eq. (12)). As a result, the change in the ambient heat-transfer condition does not simply restore the mass-spring harmonic oscillator, but introduces another resonance-like effect as shown in the following subsection.

3.2. Resonance-like heat-transfer dependence

Figure 9 shows the simulations on the field-induced deformation at different ambient heat-transfer conditions which are characterized by a time scale t_h (the characteristic heat-transfer time). The time scale t_h changes from 0.1 second (close to the isothermal condition) to 350 seconds (close to the adiabatic condition) in Fig. 9. The simulation in Fig. 6(a) takes $t_h = 68.9$ s, which corresponds to the still-air ambient condition in the experiment. The detailed measurement of t_h can be found in (Zhang et al., 2018a).

When the ambient heat transfer is very strong (e.g. $t_h = 0.1$ s in Fig. 9(a)), the specimen temperature T is always kept constant (i.e. close to the ambient temperature of 20 °C) and the output strain oscillation amplitude $\Delta\varepsilon$ is kept at a constant value of 1.7% due to the cyclic martensite reorientation (i.e. z_1 and z_2 have the oscillation amplitude of 0.29). When t_h increases (i.e. the heat transfer becomes weaker) as shown in Figs. 9(b) ~ 9(d), it takes more time for T and $\Delta\varepsilon$ to evolve to the steady state. Moreover, with the increase of t_h , both the stable temperature T_{stable} and the stable strain amplitude $\Delta\varepsilon_{stable}$ become larger: $\Delta\varepsilon_{stable} = 2.4\%$, 4.2% and 5.9% while $T_{stable} = 25.3$ °C, 30.7 °C and 38.2 °C at $t_h = 4$ s, 6 s and 12 s, respectively. For all these cases, the volume fraction of the A phase z_0 keeps at 0 (refer to Figs. 9(a) ~ 9(d)). That means, the strain oscillation is due to the cyclic Martensite Reorientation (MR), which is sensitive to the temperature (e.g., the friction-like dissipative stress σ_{tw}^{eff} decreases with increasing temperature as shown in Eq. (12)), and the temperature is influenced by the ambient heat-transfer rate (i.e. the characteristic ambient heat-transfer time t_h). For the case of $t_h = 12$ s (Fig. 9(d)), the volume fractions of the martensite variants z_1 and z_2 oscillate between 0 and 1 in the steady-state oscillation (stable cycles), implying a complete cyclic MR in the specimen.

If t_h further increases (see Figs. 9(e) ~ 9(g)), the large deformation amplitude (5.9% strain) becomes unstable when the temperature reaches around 39 °C (i.e. the characteristic phase transformation temperature $\frac{1}{2}(M_f^0 + A_f^0) \approx 39$ °C). After the strain drop (the reduction in $\Delta\varepsilon$), the temperature keeps around 39 °C for all the three cases (i.e. $t_h = 20$ s, 30 s and 100 s) where A phase and M phase coexist (the volume fraction of A phase $z_0 = 0.36$, 0.65 and 0.96 , respectively). Although their stable temperatures are almost the same, their stable strain amplitudes are different: $\Delta\varepsilon_{stable} = 3.9\%$, 2.2% and 0.3% , significantly depending on t_h due to the fact that the dissipation heat of the deformation oscillation must be balanced by the heat transferred to the ambient. That agrees with the experimental observation and the analytical calculation of the heat balance in (Zhang et al., 2018a).

When t_h further increases to 350 s (close to the adiabatic condition) in Fig. 9(h), the specimen temperature rises rapidly and becomes higher than 40 °C, making a complete M→A phase transformation ($z_0 = 1$) and a strain drop to 0 due to the lack of Martensite Reorientation (MR). In this case ($T > 40$ °C, $z_0 = 1$ and $\Delta\varepsilon = 0$), the temperature rise is solely caused by the eddy current in the material induced by the high-frequency magnetic field. Compared with the dissipation of a cyclic MR (Figs. 9(a) ~ 9(d)), the heat generated by eddy current is small (or negligible). But it can still be measured in the experiments (Pascan et al., 2016; Zhang et al. 2018a) and modelled in Eqs. (38) and (39a).

Figure 10 compares all the simulation results with the experiments in terms of the stable responses, i.e. the stable strain amplitude, the stable temperature and the stable volume fraction of A phase. The simulation covering a wide range of ambient conditions from the near-isothermal condition ($t_h = 0.1$ s) to the near-adiabatic condition ($t_h = 500$ s) agree with the experimental measurements: $\Delta\varepsilon_{stable}$ depends on t_h non-monotonically (resonance-like dependence) due to the combined effects of the temperature-dependent MR (temperature-dependent effective twinning stress σ_{tw}^{eff}) and the temperature-induced phase transformation between A phase and M phase. The wide range of the ambient dependence (t_h -dependence) can be classified into the following four domains.

(I) Close to isothermal case ($t_h \leq 1$ s):

The ambient heat exchange is so strong that the material's temperature is always kept constant (around the ambient temperature of 20 °C, well below the characteristic phase transformation temperature of about 39 °C) and only M phase exists, i.e. $z_0 = 0$. But, not all the M phase takes the reorientation in the dynamic response because the friction-like dissipative stress σ_{tw}^{eff} is high in the low temperature level, as shown in Eq. (12). Therefore, $\Delta\varepsilon_{stable}$ is not large, only around 2% in Fig. 10(a).

(II) Significant increase in $\Delta\varepsilon_{stable}$ with increasing t_h ($1 \text{ s} \leq t_h \leq 12 \text{ s}$) governed by the temperature-dependent MR process (temperature-dependent σ_{tw}^{eff}):

In this domain, the ambient heat transfer is not very strong; T_{stable} increases with increasing t_h , leading to larger $\Delta\varepsilon_{stable}$ (because of the lower MR frictional stress σ_{tw}^{eff} at higher temperature). When t_h reaches 12 s, $\Delta\varepsilon_{stable}$ reaches the maximum value of around 6% and T_{stable} reaches the material's phase transformation temperature of around 39 °C where M→A phase transformation can almost occur, i.e. z_0 starts increasing from 0.

(III) Special “isothermal” case due to the self-organized coexistence of M and A phases ($12 \text{ s} \leq t_h \leq 300 \text{ s}$):

In this domain, T_{stable} keeps almost constant (around 39 °C); but $\Delta\varepsilon_{stable}$ decreases significantly with increasing t_h due to the decreasing volume fraction of M phase (i.e. the increasing volume fraction z_0 of A phase). When t_h increases to 300 s, the material is fully occupied by A phase ($z_0 = 1$) and $\Delta\varepsilon_{stable}$ is reduced to 0 (no MR exists).

(IV) Close to adiabatic case ($t_h > 300$ s)

In this domain, the heat exchange between the specimen and the ambient is weak; the dissipation is easily accumulated to cause a large temperature rise. Therefore, T_{stable} is high (> 39 °C) and no M phase exists (i.e. no MR and $\Delta\varepsilon_{stable} = 0$). Due to the heat generated by the eddy current induced by the changing magnetic field, T_{stable} increases with t_h .

3.3. Dependence of stable strain amplitude on two time scales

The simulations in Figs. 8 and 10(a) of the previous Subsection 3.1 and 3.2 imply that the magnetic-field-induced deformation oscillation (strain amplitude $\Delta\varepsilon$) is influenced by two time scales, i.e. $\frac{1}{f_{strain}}$ and t_h , related respectively to the external magnetic driving frequency (i.e. the strain oscillation frequency $f_{strain} = 2f_{magnetic}$) and the ambient heat exchanging rate. To provide a whole picture of the dynamics of the field-induced deformation oscillation, our simulation results of the steady-state strain amplitude $\Delta\varepsilon_{stable}$ at different f_{strain} and t_h are summarized in Fig. 11, where the two time-scale axes ($\frac{1}{f_{strain}}$ and t_h) represent respectively the mass-spring dynamic effect (i.e. inertial effect) and the effect of the ambient heat-exchange (diffusion dynamics) coupled with the temperature-dependent MR and PT. It is seen from the figure that the maximum stable strain amplitude $\Delta\varepsilon_{stable}$ is obtained at the resonance time scales: $\frac{1}{f_{strain}^*} = \frac{1}{180 \text{ Hz}} = 5.56 \text{ ms}$ and $t_h^* = 12 \text{ s}$. While the resonance frequency f_{strain}^* is influenced by the mass-spring inertial effect, the resonance time scale t_h^* is governed by the balance between the heat generated by MR and the heat transferred to the ambient. Detailed experimental discussions and analytical estimation of the resonance time scale t_h^* have been provided in (Zhang et al. 2018a).

4. Discussions

4.1. Little global hysteresis between forward and reverse phase transformations

One of the interesting findings of the current study on the thermo-magneto-mechanical

coupling in Fig. 10 is the non-trivial isothermal case of $t_h = 12 \text{ s} \sim 300 \text{ s}$ where the stable strain amplitude $\Delta\varepsilon_{stable}$ changes significantly while the stable temperature T_{stable} is always constant. That proposes a special design of an isothermal actuator whose output strain amplitude can be controlled by the ambient heat transfer condition. This proposition has been experimentally verified in (Zhang et al., 2018b) as shown in Fig. 12(a) where the characteristic ambient heat-transfer time t_h was varied by changing the ambient airflow velocity from 0 m/s to 16 m/s in the stages ① ~ ⑥ (the corresponding $t_h = 68.9 \text{ s}, 29.8 \text{ s}, 23.6 \text{ s}, 16.0 \text{ s}, 13.9 \text{ s}, 12.0 \text{ s}$ from (Zhang et al., 2018a)). It is seen from the experiment (Fig. 12(a)) that in Stage ① with the still-air ambient condition, i.e. $v_{air} = 0 \text{ m/s}$, the large field-induced deformation amplitude $\Delta\varepsilon$ decreases significantly from 5.8% to 1.0% when the temperature increases to a high level (see point A in Fig. 12(a)). Then, the ambient airflow is applied in Stage ②: the strain amplitude $\Delta\varepsilon$ increases to 2.1% while the temperature reduces a little (see point B where the temperature is around 36.1 °C). It should be noted that the significant strain drop at point A is due to the M→A phase transformation (as shown in the corresponding simulation result in Fig. 12(b) where the volume fraction z_0 of A phase increases from 0) while the strain jump at point B is caused by the A→M phase transformation (z_0 decreases from 0.91 to 0.65 in Fig. 12(b)). These M→A and A→M phase transformations have also been experimentally confirmed by the observations of the microstructural evolutions in (Zhang et al., 2018b).

Both experimental observation (Fig. 12(a)) and simulation result (Fig. 12(b)) reveal that the global dynamic response of MSMA coupling phase transformation and martensite reorientation (with the simultaneous motions of numerous twin boundaries) shows little temperature hysteresis between the reverse (M→A) and the forward (A→M) martensitic Phase Transformation (PT). This contrasts with the large temperature hysteresis found from the DSC (Differential Scanning Calorimetry) measurement of the quasi-static PT in MSMA (i.e. $A_f^0 - M_f^0 = 42.2 \text{ °C} - 35.5 \text{ °C} = 6.7 \text{ °C}$ in (Zhang et al., 2018b)) and with the hysteretic-type kinetics of the common PT models (e.g. Lagoudas et al., 2006; LExcellent et al., 2000; Patoor et al., 2006; Zaki and Moumni, 2007). This global non-hysteretic phase transformation poses challenging topics for further studies with advanced experiments (e.g. in-situ ultra-fast observations of the dynamic nucleation/evolutions of the phases/variants and the associated mechanical/thermal properties) and with proper modelling (e.g. micromechanics/phase-field models linking the local twins/phases motions to the global responses).

Nevertheless, the current macroscopic model with the linear kinetics of phase transformation (without hysteresis as shown in Fig. 2(a)) can capture all the main features of

the global dynamic behaviors of MSMA as shown by the simulation results in Section 3 and this subsection 4.1. On the contrary, the simulation with the hysteretic-type kinetics (Fig. 2(b)) is shown in Fig. 12(c), which does not agree with the experimental observation in Fig. 12(a):

- (1) The difference between the simulated steady-state temperature after the strain amplitude drop in Stage ① and that after the strain amplitude jump in Stage ② is significant, i.e. $41.7\text{ }^{\circ}\text{C} - 36.5\text{ }^{\circ}\text{C} = 5.2\text{ }^{\circ}\text{C}$ in Fig. 12(c), while the corresponding temperature difference in both Figs. 12(a) and 12(b) is small, i.e. $< 0.5\text{ }^{\circ}\text{C}$.
- (2) In Fig. 12(c), due to the hysteresis effect, the ①→② ambient change at t_1 does not trigger the immediate $\Delta\varepsilon$ increase. In fact, the increase in $\Delta\varepsilon$ is delayed by almost 20 s (see point A in Fig. 12(c) where z_0 starts to decrease from 0.85 to 0.74). On the contrary, both Figs. 12(a) and 12(b) show the immediate effect of the ①→② ambient change on $\Delta\varepsilon$ at t_1 .

The above discussions indicate that, although the localized quasi-static temperature-induced or stress-induced phase transformation in MSMA is hysteretic (e.g. DSC measurement in (Zhang et al., 2018b) and mechanical tests in (Martynov and Kokorin, 1992)), the observed global dynamic phase transformation in the inhomogeneous system of MSMA (i.e. including simultaneous nucleation/motion of numerous phases/boundaries) has little hysteresis.

4.2. Quantification on global phase transformation speed

Besides the quality of the global phase transformation (better described/simulated with a linear kinetics rather than a hysteretic-type kinetics), the quantification on the global phase transformation speed is surprising in the current study. For example, Fig. 13 shows the simulated effect of the latent heat absorption (ΔH) on the speed of the M→A phase transformation (z_0 increases from 0 to 0.91) during the strain-amplitude drop ($\Delta\varepsilon$ decreases from 5.9% to 0.6%). It is seen that the time Δt_{drop} for the strain drop (due to the M→A phase transformation) increases almost proportionally with ΔH : Δt_{drop} increases from 4 s to 79 s (nearly 20-fold increase) when ΔH increases from $5.39 \times 10^6\text{ J} \cdot \text{m}^{-3}$ to $1.08 \times 10^8\text{ J} \cdot \text{m}^{-3}$ (20-fold increase). This proportional dependence is due to the heat balance between the latent heat adsorption of the M→A phase-transformation, the heat generation from the eddy current and the dissipation of martensite reorientation and phase transformation, and the ambient heat transfer as modelled in Eqs. (37) and (38). The surprising point is that, if ΔH takes the value ($5.39 \times 10^7\text{ J} \cdot \text{m}^{-3}$) measured from the DSC test in (Zhang et al., 2018b), the simulated time of the strain drop (i.e. $\Delta t_{drop} \approx 36\text{ s}$ in Fig. 13(c)) is much longer than the experimental observation ($\Delta t_{drop} \approx 5\text{ s}$) in Fig 6(b). In order to understand this disagreement and double-

check the time scale, we perform the following simple cycle-average heat analysis based on the heat balance equation from Eq. (37):

$$\frac{dT}{dt} = \frac{1}{\lambda} (r_{MR} + r_{PT} + r_{eddy}) - \frac{(T-T_0)}{t_h} \quad (44)$$

where $t_h = \frac{\lambda R}{2h} = 68.9$ s (for the still-air ambient condition); r_{MR} , r_{PT} and r_{eddy} are respectively the heat generation rate due to the Martensite-Reorientation dissipation, the rate of the dissipation (D_p) and the latent heat adsorption ($-\Delta H$) due to the M→A Phase Transformation (PT), and the heat generation rate due to the eddy current power loss, which are expressed in cycle-average forms of the current case (with $f_{strain} = 180$ Hz and near the constant temperature $T = 39.2$ °C close to A_s^0 during the strain drop) as:

$$r_{MR} = 2f_{strain}\sigma_{tw}^{eff}\varepsilon_0(1 - z_0) = b_1(1 - z_0) \quad (45a)$$

$$r_{PT} = (D_p - \Delta H)\frac{dz_0}{dt} = b_2\frac{dz_0}{dt} \quad (45b)$$

$$r_{eddy} = 2320.7f_{strain} - 1.35 \times 10^5 = 2.83 \times 10^5 \text{ W} \cdot \text{m}^{-3} \quad (45c)$$

with $b_1 = 2f_{strain}\sigma_{tw}^{eff}\varepsilon_0 \approx 2 \times 180 \text{ Hz} \times 0.2 \text{ MPa} \times 6\% = 4.32 \times 10^6 \text{ W} \cdot \text{m}^{-3}$, using Eq. (14) and assuming all the existing martensite takes reorientation (a complete MR) like the case in Fig. 13 ($\varepsilon_0 = \Delta\varepsilon_{unstable} = 5.9\% \approx 6\%$); $b_2 = D_p - \Delta H \approx -\Delta H$, because $|\Delta H| \gg D_p$ whose value is given in Table 1. Since the calculated r_{eddy} in Eq. (45c) is much smaller than b_1 , we ignore r_{eddy} and substitute Eqs. (45a) and (45b) into Eq. (44) to describe the strain drop (in term of the increase in the A-phase volume fraction z_0) near the constant temperature A_s^0 (i.e. $\frac{dT}{dt} = 0$):

$$b_1(1 - z_0) + b_2\frac{dz_0}{dt} - b_3 = 0 \quad (46)$$

where $b_3 = \frac{\lambda(A_s - T_0)}{t_h}$. The solution to Eq. (46) is:

$$z_0 = C_1 e^{-\frac{1}{t_{PT}}t} + \frac{b_1 - b_3}{b_1} \quad (47)$$

where C_1 is a constant determined by the initial condition; the characteristic phase transformation time (relaxation time) $t_{PT} = -\frac{b_2}{b_1} \approx \frac{\Delta H}{b_1} = 12.5$ s (using $\Delta H = 5.39 \times 10^7 \text{ J} \cdot \text{m}^{-3}$ measured in the DSC test of (Zhang et al., 2018b)). Normally, it takes around 3 times of the characteristic time scale to finish a relaxation process, i.e. strain drop in the current case. Therefore, the duration Δt_{drop} of the strain drop can be estimated as $\Delta t_{drop} \approx 3t_{PT} = 37.5$ s, which agrees with the simulation result in Fig. 13(c) where $\Delta t_{drop} \approx 36$ s, but does not agree with the experimental observation in Fig. 6(b) where $\Delta t_{drop} \approx 5$ s. That means, both the

simple analysis above and the numerical simulation in Fig. 13(c) demonstrate the limitation of the macroscopic model about the quantification on the global dynamic phase transformation speed.

The reason for this limitation might be that the macroscopic model describing the lumped sum of the inhomogeneous physical fields in the system containing various phases/variants is weak to capture some instability behaviours like phase nucleation. For example, the temperature T , as a system's global state variable in the model, is just the average temperature of the inhomogeneous MSMA system where the phase-transformation-induced self-heating (due to dissipation) and self-cooling (due to latent heat absorption) are localized, especially during the nucleation (appearance) of a new phase (i.e. z_0 starts to increase from 0). The nucleation of new phases during phase transformations in traditional Shape Memory Alloys (SMA) has been well studied in the literature. For example, the stress-induced martensitic phase transformation triggers the Lüders-like band formation (for the nucleation of the new phase), which indicates that the phase transformation does not take place uniformly in a SMA specimen, but is concentrated at certain parts of the specimen, causing strain concentration and localized heating/cooling (Shaw and Kyriakides, 1995, 1997; Zhang and He, 2018; Zheng et al., 2016). Particularly, the appearance of the new phase (phase nucleation) is an avalanche-like unstable process causing the macroscopic (global) stress drop; such global stress drop is not obvious in some dynamic loading conditions (He and Sun, 2010b; Zhang et al., 2010). Similarly, in the current experiment on magnetic SMA, the temperature-induced $M \rightarrow A$ phase transformation during the strain drop is accompanied with a temperature drop as indicated in Fig. 6(b). It should be noted that in the experiments of (Zhang et al., 2018a), a thermocouple attaching to the specimen's end to measure the temperature T might not accurately capture the peak (maximum) temperature in the specimen. In other words, the motion of numerous twin boundaries causes localized heating (due to the MR dissipation) leads to an inhomogeneous temperature distribution in the specimen, triggering the localized $M \rightarrow A$ phase transformation (when the local temperature reaches A_s^0 or A_f^0). Then the avalanche-like $M \rightarrow A$ phase transformation adsorbs large latent heat, reducing the temperature significantly, i.e. the temperature is reduced to be close to but higher than M_s^0 or M_f^0 to avoid the reverse $A \rightarrow M$ phase transformation. This has been confirmed by many tests in (Zhang et al. 2018a) as shown in Fig. 14 where the tests with strain drop (i.e. with $M \rightarrow A$ phase transformation) have a global stable temperature around M_s^0 (36.5 °C) and M_f^0 (35.5 °C).

Based on this physical picture about the avalanche-like phase transformation (the strain drop is accompanied with the temperature drop), we can make a rough estimation of the required time ($\Delta t_{drop-avalanche}$) for the strain-drop process (M \rightarrow A phase transformation) by using the heat balance equation (Eq. (44)) and assuming the relaxation-type evolutions (“drops”) of T and z_0 as:

$$z_0 = A_1 e^{-\frac{t}{\tau}} + A_2 \quad (48a)$$

$$T = A_3 e^{-\frac{t}{\tau}} + A_4 \quad (48b)$$

where τ is a characteristic relaxation time scale to be determined; the constants $A_1 \sim A_4$ can be determined by the following initial/boundary conditions of the strain drop process:

- At $t = 0$, $z_0 = 0$ and $T \approx A_f^0 = 42.2$ °C
- At $t \rightarrow \infty$, $z_0 \approx \frac{\varepsilon_0 - \Delta\varepsilon_{stable}}{\varepsilon_0} = 0.83$ (from the experiment in Fig. 6(b)) and $T \approx M_f^0 = 35.5$ °C (from the DSC measurement in (Zhang et al., 2018b))

from which the constants in Eq. (48) can be determined as: $A_1 = -0.83$, $A_2 = 0.83$, $A_3 = 6.7$ °C and $A_4 = 35.5$ °C. With Eqs. (45) and (48), we integrate Eq. (44) in the time period $[0, 3\tau]$ to satisfy the total heat balance in the whole strain-drop process:

$$\int_0^{3\tau} \frac{dT}{dt} dt = \int_0^{3\tau} \left(\frac{1}{\lambda} (r_{MR} + r_{PT}) - \frac{(T-T_0)}{t_h} \right) dt$$

Then the characteristic relaxation time scale τ can be determined as:

$$\tau = \frac{\left(A_3 + \frac{\Delta H}{\lambda} A_1 \right) (e^{-3} - 1)}{\frac{b_1}{\lambda} (3(1-A_2) + A_1(e^{-3}-1)) + \frac{A_3}{t_h} (e^{-3}-1) + \frac{3(T_0-A_4)}{t_h}} \quad (49)$$

The parameter b_1 in Eq. (49) can be determined from Eq. (45a) where the effective twinning stress σ_{tw}^{eff} depends on the temperature: we take $T \approx \frac{1}{2} (A_f^0 + M_f^0) \approx 39$ °C and use Eq. (14) to find $\sigma_{tw}^{eff} = 0.26$ MPa. So $b_1 = 2f_{strain} \sigma_{tw}^{eff} \varepsilon_0 \approx 2 \times 180 \text{ Hz} \times 0.26 \text{ MPa} \times 6\% = 5.62 \times 10^6 \text{ W} \cdot \text{m}^{-3}$. By introducing the values of the related parameters into Eq. (49), we determine the characteristic time scale as: $\tau \approx 4$ s. Then the time of the strain drop can be roughly estimates as: $\Delta t_{drop-avalanche} \approx 3\tau = 12$ s, close to the experimental observation in Fig. 6(b) where $\Delta t_{drop} \approx 5$ s.

That means, due to the avalanche-like nucleation of phase transformation, the strain drop is accompanied with a temperature drop from A_s^0 (or A_f^0) to M_s^0 (or M_f^0). With such temperature drop, the latent heat absorption of the M \rightarrow A phase transformation can be provided/balanced quickly. That’s why the experimentally-observed M \rightarrow A phase transformation speed during the strain drop can be faster than the expectation (the simulation

result in Fig. 13(c)). As a phenomenological model, the current simulation adopts the value of the apparent latent heat $\Delta H_{apparent} = 1.08 \times 10^7 \text{ J} \cdot \text{m}^{-3}$ (about one fifth of the experimentally-measured value of $\Delta H_{DSC-test} = 5.39 \times 10^7 \text{ J} \cdot \text{m}^{-3}$) to describe strain drop process in Section 3.

Moreover, the temperature drop from A_s^0 (or A_f^0) to M_s^0 (or M_f^0) can explain the little hysteresis between the forward and reverse phase transformations discussed in Section 4.1. After the strain drop process with the avalanche-like $M \rightarrow A$ phase transformation causing the temperature drop, the specimen's temperature is already very close to M_s^0 (or M_f^0). Therefore, just a small cooling (e.g. by the ambient airflow in Stage ② in Fig. 12(a)) is enough to immediately trigger the $A \rightarrow M$ phase transformation, showing apparently little hysteresis.

5. Summary and conclusions

This paper develops a dynamic model to study the thermo-magneto-mechanical coupling behaviours of Magnetic Shape Memory Alloys (MSMA) actuated by high-frequency magnetic fields under various thermal conditions. Our previous constitutive model focusing on martensite reorientation in MSMA is extended to the current model to describe the coupling between the temperature-dependent field-induced dissipative martensite reorientation and the temperature-induced forward/reverse martensitic phase transformation. The extended constitutive model is further embedded in a mass-spring dynamic configuration to study and understand the new experimental dynamic phenomena. Comparisons between experimental observations and model simulations (with different kinetics of phase transformation) demonstrate that the dynamic forward/reverse martensitic phase transformation shows little hysteresis, contrasting to the quasi-static cases. Detailed quantitative discussion on the time scale of the transient phase transformation process further reveals that the phase transformation, due to the coupling dynamics, leads to sudden changes in both deformation and temperature (i.e. strain-amplitude drop is accompanied with a temperature drop) even though the current experiments have not yet measured the temperature drop accurately. Three main conclusions are drawn from the study:

- (1) Due to the coupling of the martensite reorientation and the phase transformation, the mechanical deformation (strain oscillation) depends on both the magnetic loading and the thermal condition; particularly, the optimized performance (maximum stable strain

amplitude) can be achieved only at the critical magnetic driving frequency and the critical ambient heat-exchange rate, which are characterized by the two time scales ($\frac{1}{f_{strain}}$ and t_h in Fig. 11) representing the effects of the inertial dynamics and the heat balance, respectively.

- (2) Generally, the higher the heat exchanging rate between the ambient and the MSMA system (with the field-induced dissipative martensite reorientation), the lower the stable system temperature. But, the system temperature does not totally change with the ambient condition in a passive way. In a certain range of the ambient conditions (such as $12 \text{ s} \leq t_h \leq 300 \text{ s}$ in Fig. 10), the self-organized microstructure (self-adjusted volume fractions of the martensite and the austenite) leads to a special “isothermal” behaviour — the temperature keeps constant while the strain oscillation amplitude (due to the cyclic field-induced martensite reorientation) changes significantly with the ambient condition. In other words, the MSMA system can be smart to keep its temperature constant by self-organization under the varying external thermo-magneto-mechanical boundary conditions.
- (3) The global kinetics of the phase transformation in a dynamic MSMA system containing simultaneous multiple nucleation/motions of the phases/boundaries under the thermo-magneto-mechanical dynamic loadings is significantly different from that of the quasi-static phase transformation (such as that in the DSC measurement). Particularly, contrasting with the well-known hysteresis (e.g. the temperature hysteresis of $(A_f^0 - M_f^0)$ from a DSC measurement), the global dynamic phase transformation has little hysteresis and can be phenomenologically modelled with a simple linear kinetics in Fig. 12.

Appendix A. Magnetic susceptibility of martensite variants

The magnetic susceptibility a_i ($i = 1, 2, 3$) of the three pseudo-tetragonal 5M martensite variants of Ni-Mn-Ga single crystal in the magnetic energy formulation (Eq. (2c)) reflects the overall effects of the magnetic-domain-wall motions and local magnetization rotations on the global magnetization process (Likhachev and Ullakko, 2000). Two magnetization tests are needed to determine a_1, a_2, a_3 : one along the magnetic easy-axis of the martensite variant and the other along the hard-axis (see Fig. A.1). It is noted that the magnetic easy-axis is parallel

to the short c -axis of the pseudo-tetragonal 5M martensite of Ni-Mn-Ga single crystal and the hard-axis is perpendicular to it.

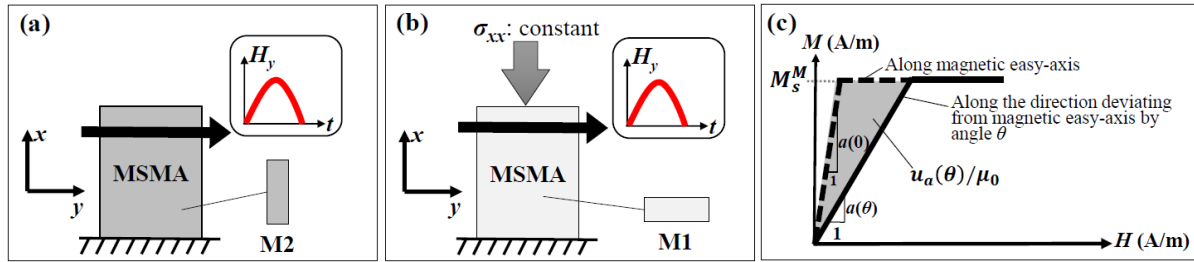


Fig. A.1. (a) Magnetization test along magnetic easy-axis. (b) Magnetization test along magnetic hard-axis with a large compressive stress σ_{xx} . (c) Magnetization curves (after linear approximation) of the magnetization along the magnetic easy-axis (dashed line) and that along the direction deviating from the easy-axis by an angle θ (solid line). The uniaxial magneto-crystalline anisotropy energy $u_a(\theta)$ can be determined by the area between the two magnetization curves. The saturation magnetization M_s^M and the magnetic susceptibilities $a(0)$ and $a(\theta)$ are also indicated.

(a) Magnetization test along magnetic easy-axis (Fig. A.1(a))

The sample in the state of single martensite variant with magnetic easy-axis along y -coordinate is magnetized by a magnetic field H_y . By linearization of the magnetization curve (see Fig. A.1(c)), we can determine the saturation magnetization M_s^M and the magnetic susceptibility $a(0)$ for the magnetization along the magnetic easy-axis.

(b) Magnetization along magnetic hard-axis (Fig. A.1(b))

The sample in the state of single martensite variant with magnetic easy axis along x -coordinate is magnetized by a magnetic field H_y . To prevent martensite reorientation during the experiment, a large constant compressive stress σ_{xx} is applied along x -coordinate. Following the same procedures as the previous experiment, the magnetization curve for the magnetization process along the magnetic hard-axis is obtained.

The uniaxial magneto-crystalline anisotropy energy density u_a for Ni-Mn-Ga 5M martensite can be expressed as (O'Handley et al., 2000):

$$u_a(\theta) = K_u \sin^2 \theta \quad (\text{A.1})$$

where K_u is the coefficient of magneto-crystalline anisotropy energy; θ is the equilibrium angle between the magnetic easy-axis of the martensite variant and its magnetization vector. $u_a(\theta)$ can be determined by the area between the magnetization curve along the easy-axis and that along the direction deviating by an angle θ from the easy-axis (see the shaded area in Fig. A.1(c)). For the magnetization along the magnetic hard-axis ($\theta = \pi/2$), we have $u_a = K_u$. So K_u can be directly obtained by the magnetization curves from the previous two magnetization tests. From Fig. A.1(c), $u_a(\theta)$ can be calculated as:

$$u_a(\theta) = \frac{1}{2}\mu_0(M_s^M)^2 \left(\frac{1}{a(\theta)} - \frac{1}{a(0)} \right) \quad (\text{A.2})$$

where $a(0)$ and $a(\theta)$ are respectively the magnetic susceptibilities of the magnetization along the magnetic easy-axis ($\theta = 0$) and that along the direction deviating by an angle θ from the easy-axis. With Eqs. (A.1) and (A.2), we can obtain the following expression of $a(\theta)$:

$$a(\theta) = \left(\frac{1}{a(0)} + \frac{2K_u \sin^2 \theta}{\mu_0(M_s^M)^2} \right)^{-1} \quad (\text{A.3})$$

The magnetic easy-axes for variants 1, 2 and 3 are respectively the x -, y - and z -coordinate. Let θ_1 , θ_2 and θ_3 be the angles between the magnetic field \underline{H} and the x -, y -, z -coordinate, respectively. By Eq. (A.3), the magnetic susceptibilities of the martensite variants are:

$$a_i = \left(\frac{1}{a(0)} + \frac{2K_u \sin^2 \theta_i}{\mu_0(M_s^M)^2} \right)^{-1} \quad \text{for variant } i \quad (i = 1, 2, 3) \quad (\text{A.4})$$

References

- Aharoni, A., 1998. Demagnetizing factors for rectangular ferromagnetic prisms. *J. Appl. Phys.* 83, 3432–3434.
- Asua, E., García-Arribas, A., Etxebarria, V., Feuchtwanger, J., 2014. Pulsed-mode operation and performance of a ferromagnetic shape memory alloy actuator. *Smart Mater. Struct.* 23, 025023.
- Auricchio, F., Bonetti, E., Scalet, G., Ubertini, F., 2014. Theoretical and numerical modeling of shape memory alloys accounting for multiple phase transformations and martensite reorientation. *Int. J. Plasticity* 59, 30–54.
- Bhattacharya, K., 2003. *Microstructure of Martensite*, Oxford University Press, New York.
- Bruno, N.M., Wang, S., Karaman, I., Chumlyakov, Y.I., 2016. Reversible martensitic transformation under low magnetic fields in magnetic shape memory alloys. *Sci. Rep.* 7, 40434.
- Chen, X., He, Y., Moumni, Z., 2013. Twin boundary motion in NiMnGa single crystals under biaxial compression. *Mater. Lett.* 90, 72–75.
- Chen, X., Moumni, Z., He, Y., Zhang, W., 2014. A three-dimensional model of magneto-mechanical behaviors of martensite reorientation in ferromagnetic shape memory alloys. *J. Mech. Phys. Solids* 64, 249–286.
- Cisse, C., Zaki, W., Zineb, T.B., 2016. A review of constitutive models and modeling techniques for shape memory alloys. *Int. J. Plasticity* 76, 244–284.

- Faran, E., Shilo, D., 2011. The kinetic relation for twin wall motion in NiMnGa. *J. Mech. Phys. Solids* 59, 975–987.
- Faran, E., Shilo, D., 2012. Implications of twinning kinetics on the frequency response in NiMnGa actuators. *Appl. Phys. Lett.* 100, 151901.
- Faran, E., Shilo, D., 2013. The kinetic relation for twin wall motion in NiMnGa—part 2. *J. Mech. Phys. Solids* 61, 726–741.
- Faran, E., Riccardi, L., Shilo, D., 2017. Inertia-controlled twinning in Ni–Mn–Ga actuators: a discrete twin-boundary dynamics study. *Shape Mem. Superelasticity* 3, 206–217.
- Faran, E., Shilo, D., 2016. A discrete twin-boundary approach for simulating the magneto-mechanical response of Ni–Mn–Ga. *Smart Mater. Struct.* 25, 095020.
- Gauthier, J.Y., 2007. Modélisation des alliages à mémoire de forme magnétiques pour la conversion d'énergie dans les actionneurs et leur commande. Ph.D. thesis, Université de Franche-Comté, France.
- Haldar, K., Kiefer, B., Lagoudas, D.C., 2011. Finite element analysis of the demagnetization effect and stress inhomogeneities in magnetic shape memory alloy samples. *Philos. Mag.* 91, 4126–4157.
- Haldar, K., Lagoudas, D.C., 2018. Dynamic magnetic shape memory alloys responses: eddy current effect and Joule heating. *J. Magn. Magn. Mater.* 465, 278–289.
- Haldar, K., Lagoudas, D.C., Karaman, I., 2014. Magnetic field-induced martensitic phase transformation in magnetic shape memory alloys: modeling and experiments. *J. Mech. Phys. Solids* 69, 33–66.
- He, Y.J., Chen, X., Moumni, Z., 2011. Two-dimensional analysis to improve the output stress in ferromagnetic shape memory alloys. *J. Appl. Phys.* 110, 063905.
- He, Y.J., Chen, X., Moumni, Z., 2012. Reversible-strain criteria of ferromagnetic shape memory alloys under cyclic 3D magneto-mechanical loadings. *J. Appl. Phys.* 112, 033902.
- He, Y.J., Sun, Q.P., 2010a. Frequency-dependent temperature evolution in NiTi shape memory alloy under cyclic loading. *Smart Mater. Struct.* 19, 115014.
- He, Y.J., Sun, Q.P., 2010b. Rate-dependent domain spacing in a stretched NiTi strip. *Int. J. Solids Struct.* 47, 2775–2783.
- He, Y.J., Sun, Q.P., 2011. On non-monotonic rate dependence of stress hysteresis of superelastic shape memory alloy bars. *Int. J. Solids Struct.* 48, 1688–1695.
- Heczko, O., 2005a. Determination of ordinary magnetostriction in Ni–Mn–Ga magnetic shape memory alloy. *J. Magn. Magn. Mater.* 290–291, 846–849.

- Heczko, O., 2005b. Magnetic shape memory effect and magnetization reversal. *J. Magn. Magn. Mater.* 290–291, 787–794.
- Heczko, O., Lanska, N., Soderberg, O., Ullakko, K., 2002. Temperature variation of structure and magnetic properties of Ni–Mn–Ga magnetic shape memory alloys. *J. Magn. Magn. Mater.* 242–245, 1446–1449.
- Heczko, O., Sozinov, A., Ullakko, K., 2000. Giant field-induced reversible strain in magnetic shape memory NiMnGa alloy. *IEEE Trans. Magn.* 36, 3266–3268.
- Henry, C.P., 2002. Dynamic actuation properties of Ni–Mn–Ga ferromagnetic shape memory alloys. Ph.D. thesis, Massachusetts Institute of Technology, USA.
- Hobza, A., Patrick, C.L., Ullakko, K., Rafla, N., Lindquist, P., Müllner, P., 2018. Sensing strain with Ni-Mn-Ga. *Sens. Actuators A.* 269, 137–144.
- Jin, Y.M., 2009. Domain microstructure evolution in magnetic shape memory alloys: phase-field model and simulation. *Acta Mater.* 57, 2488–2495.
- Kainuma, R., Imano, Y., Ito, W., Sutou, Y., Morito, H., Okamoto, S., Kitakami, O., Oikawa, K., Fujita, A., Kanomata, T., Ishida, K., 2006. Magnetic-field-induced shape recovery by reverse phase transformation. *Nature* 439, 957–960.
- Karaca, H.E., Karaman, I., Basaran, B., Chumlyakov, Y.I., Maier, H.J., 2006. Magnetic field and stress induced martensite reorientation in NiMnGa ferromagnetic shape memory alloy single crystals. *Acta Mater.* 54, 233–245.
- Karaca, H.E., Karaman, I., Basaran, B., Ren, Y., Chumlyakov, Y.I., Maier, H.J., 2009. Magnetic field-induced phase transformation in NiMnCoIn magnetic shape-memory alloys—a new actuation mechanism with large work output. *Adv. Funct. Mater.* 19, 983–998.
- Kiefer, B., Lagoudas, D.C., 2005. Magnetic field-induced martensitic variant reorientation in magnetic shape memory alloys. *Philos. Mag.* 85, 4289–4329.
- Kiefer, B., Lagoudas, D.C., 2009. Modeling the coupled strain and magnetization response of magnetic shape memory alloys under magnetomechanical loading. *J. Intell. Mater. Syst. Struct.* 20, 143–170.
- Kohl, M., Gueltig, M., Pinneker, V., Yin, R., Wendler, F., Krevet, B., 2014. Magnetic shape memory microactuators. *Micromachines* 5, 1135–1160.
- Kohl, M., Srinivasa Reddy, Y., Khelifaoui, F., Krevet, B., Backen, A., Fähler, S., Eichhorn, T., Jakob, G., Mecklenburg, A., 2010. Recent progress in FSMA microactuator developments. *Mater. Sci. Forum* 635, 145–154.

- Krevet, B., Kohl, M., Morrison, P., Seelecke, S., 2008. Magnetization- and strain-dependent free energy model for FEM simulation of magnetic shape memory alloys. *Eur. Phys. J. Spec. Top.* 158, 205–211.
- Lagoudas, D.C., Entchev, P.B., Popov, P., Patoor, E., Brinson, L.C., Gao, X., 2006. Shape memory alloys, Part II: modeling of polycrystals. *Mech. Mater.* 38, 430–462.
- Lai, Y.W., 2009. Magnetic microstructure and actuation dynamics of NiMnGa magnetic shape memory materials. Ph.D. thesis, Technische Universität Dresden, Germany.
- Lai, Y.W., Schäfer, R., Schultz, L., McCord, J., 2008. Direct observation of AC field-induced twin-boundary dynamics in bulk NiMnGa. *Acta Mater.* 56, 5130–5137.
- Lexcellent, C., Leclercq, S., Gabry, B., Bourbon, G., 2000. The two way shape memory effect of shape memory alloys: an experimental study and a phenomenological model. *Int. J. Plasticity* 16, 1155–1168.
- Li, L.J., Lei, C.H., Shu, Y.C., Li, J.Y., 2011. Phase-field simulation of magnetoelastic couplings in ferromagnetic shape memory alloys. *Acta Mater.* 59, 2648–2655.
- Likhachev, A.A., Ullakko, K., 2000. Magnetic-field-controlled twin boundaries motion and giant magneto-mechanical effects in Ni–Mn–Ga shape memory alloy. *Phys. Lett. A* 275, 142–151.
- Martynov, V.V., Kokorin, V.V., 1992. The crystal structure of thermally- and stress-induced martensites in Ni₂MnGa single crystals. *J. Phys. III France* 2, 739–749.
- Morrison, P., Seelecke, S., Krevet, B., Kohl, M., 2008. A free energy model for magneto-mechanically coupled NiMnGa single crystals. *Eur. Phys. J. Spec. Top.* 158, 213–220.
- Murray, S.J., Marioni, M., Allen, S.M., O’Handley, R.C., Lograsso, T.A., 2000. 6% magnetic-field-induced strain by twin-boundary motion in ferromagnetic Ni–Mn–Ga. *Appl. Phys. Lett.* 77, 886–888.
- Nemat-Nasser, S., Choi, J.-Y., Guo, W.-G., Isaacs, J.B., 2005. Very high strain-rate response of a NiTi shape-memory alloy. *Mech. Mater.* 37, 287–298.
- O’Handley, R.C., Murray, S.J., Marioni, M., Nembach, H., Allen, S.M., 2000. Phenomenology of giant magnetic-field-induced strain in ferromagnetic shape-memory materials. *J. Appl. Phys.* 87, 4712–4717.
- Pascan, O.-Z., 2015. Dynamic behaviors of ferromagnetic shape memory alloys. Ph.D. thesis, ENSTA ParisTech, France.
- Pascan, O.-Z., He, Y.J., Moumni, Z., Zhang, W.H., 2015. Temperature rise of high-frequency martensite reorientation via Type II twin boundary motion in NiMnGa ferromagnetic shape memory alloy. *Scripta Mater.* 104, 71–74.

- Pascan, O.-Z., He, Y., Moumni, Z., Zhang, W., 2016. High-frequency performance of ferromagnetic shape memory alloys. *Ann. Solid Struct. Mech.* 8, 17–25.
- Patoor, E., Lagoudas, D.C., Entchev, P.B., Brinson, L.C., Gao, X., 2006. Shape memory alloys, Part I: general properties and modeling of single crystals. *Mech. Mater.* 38, 391–429.
- Peng, Q., He, Y.J., Moumni, Z., 2015. A phase-field model on the hysteretic magneto-mechanical behaviors of ferromagnetic shape memory alloy. *Acta Mater.* 88, 13–24.
- Rogovoy, A., Stolbova, O., 2016. Modeling the magnetic field control of phase transition in ferromagnetic shape memory alloys. *Int. J. Plasticity* 85, 130–155.
- Sarawate, N., Dapino, M., 2008. Frequency dependent strain-field hysteresis model for ferromagnetic shape memory Ni–Mn–Ga. *IEEE Trans. Magn.* 44, 566–575.
- Shaw, J.A., Kyriakides, S., 1995. Thermomechanical aspects of NiTi. *J. Mech. Phys. Solids* 43, 1243–1281.
- Shaw, J.A., Kyriakides, S., 1997. On the nucleation and propagation of phase transformation fronts in a NiTi alloy. *Acta Mater.* 45, 683–700.
- Sozinov, A., Lanska, N., Soroka, A., Straka, L., 2011. Highly mobile type II twin boundary in Ni-Mn-Ga five-layered martensite. *Appl. Phys. Lett.* 99, 124103.
- Sozinov, A., Likhachev, A.A., Lanska, N., Ullakko, K., 2002. Giant magnetic-field-induced strain in NiMnGa seven-layered martensitic phase. *Appl. Phys. Lett.* 80, 1746–1748.
- Stephan, J.M., Pagounis, E., Laufenberg, M., Paul, O., Ruther, P., 2011. A novel concept for strain sensing based on the ferromagnetic shape memory alloy NiMnGa. *IEEE Sens. J.* 11, 2683–2689.
- Straka, L., Heczko, O., Seiner, H., Lanska, N., Drahokoupil, J., Soroka, A., Fähler, S., Hänninen, H., Sozinov, A., 2011. Highly mobile twinned interface in 10 M modulated Ni-Mn-Ga martensite: Analysis beyond the tetragonal approximation of lattice. *Acta Mater.* 59, 7450–7463.
- Straka, L., Lanska, N., Ullakko, K., Sozinov, A., 2010. Twin microstructure dependent mechanical response in Ni-Mn-Ga single crystals. *Appl. Phys. Lett.* 96, 131903.
- Straka, L., Soroka, A., Seiner, H., Hänninen, H., Sozinov, A., 2012. Temperature dependence of twinning stress of Type I and Type II twins in 10M modulated Ni–Mn–Ga martensite. *Scripta Mater.* 67, 25–28.
- Techapiesanchaenroj, R., Kostamo, J., Allen, S.M., O’Handley, R.C., 2009. Frequency response of acoustic-assisted Ni–Mn–Ga ferromagnetic-shape-memory-alloy actuator. *J. Appl. Phys.* 105, 093923.

- Techapiesancharoenkij, R., Kostamo, J., Allen, S.M., O'Handley, R.C., 2011. The effect of magnetic stress and stiffness modulus on resonant characteristics of Ni–Mn–Ga ferromagnetic shape memory alloy actuators. *J. Magn. Magn Mater.* 323, 3109–3116.
- Ullakko, K., Huang, J.K., Kantner, C., O'Handley, R.C., Kokorin, V.V., 1996. Large magnetic-field-induced strains in Ni₂MnGa single crystals. *Appl. Phys. Lett.* 69, 1966–1968.
- Wang, J., Steinmann, P., 2012. A variational approach towards the modelling of magnetic field-induced strains in magnetic shape memory alloys. *J. Mech. Phys. Solids* 60, 1179–1200.
- Wu, P.P., Ma, X.Q., Zhang, J.X., Chen, L.Q., 2011. Phase-field simulations of magnetic field-induced strain in Ni₂MnGa ferromagnetic shape memory alloy. *Philos. Mag.* 91, 2102–2116.
- Yin, R., Wendler, F., Krevet, B., Kohl, M., 2016. A magnetic shape memory microactuator with intrinsic position sensing. *Sens. Actuators A* 246, 48–57.
- Yu, C., Kang, G., Fang, D., 2018. A thermo-magneto-mechanically coupled constitutive model of magnetic shape memory alloys. *Acta Mech. Solida Sin.* 31, 535–556.
- Yu, C., Kang, G., Song, D., Xie, X., 2019. Three-dimensional constitutive model for magneto-mechanical deformation of NiMnGa ferromagnetic shape memory alloy single crystals. *Acta Mech. Sin.*, <https://doi.org/10.1007/s10409-018-0816-6>.
- Zaki, W., Moumni, Z., 2007. A three-dimensional model of the thermomechanical behaviour of shape memory alloys. *J. Mech. Phys. Solids* 55, 2455–2490.
- Zhang, S., Chen, X., Moumni, Z., He, Y., 2018a. Thermal effects on high-frequency magnetic-field-induced martensite reorientation in ferromagnetic shape memory alloys: an experimental and theoretical investigation. *Int. J. Plasticity* 108, 1–20.
- Zhang, S., Chen, X., Moumni, Z., He, Y., 2018b. Coexistence and compatibility of martensite reorientation and phase transformation in high-frequency magnetic-field-induced deformation of Ni–Mn–Ga single crystal. *Int. J. Plasticity* 110, 110–122.
- Zhang, S., He, Y., 2018. Fatigue resistance of branching phase-transformation fronts in pseudoelastic NiTi polycrystalline strips. *Int. J. Solids Struct.* 135, 233–244.
- Zhang, X., Feng, P., He, Y., Yu, T., Sun, Q., 2010. Experimental study on rate dependence of macroscopic domain and stress hysteresis in NiTi shape memory alloy strips. *Int. J. Mech. Sci.* 52, 1660–1670.
- Zheng, L., He, Y., Moumni, Z., 2016. Effects of Lüders-like bands on NiTi fatigue behaviors. *Int. J. Solids Struct.* 83, 28–44.
- Zreihan, N., Faran, E., Shilo, D., 2018. The effect of loading rate on characteristics of type II twin boundary motion in Ni–Mn–Ga. *Scripta Mater.* 144, 44–47.

Table 1. Values of model parameters.

a_0	Magnetic susceptibility of austenite	6×10^2 (Heczko, 2005b)	M_S^A	Saturation magnetization of austenite	$3.9 \times 10^5 \text{ A} \cdot \text{m}^{-1}$ (Heczko, 2005b)
a_1	Magnetic susceptibility of martensite variant 1	0.95 (Heczko, 2005b)	M_S^M	Saturation magnetization of martensite	$5 \times 10^5 \text{ A} \cdot \text{m}^{-1}$ (Heczko, 2005b)
a_2	Magnetic susceptibility of martensite variant 2	5×10^2 (Heczko, 2005b)	N	Demagnetization factor	0.55 *
A_S^0	Austenite start temperature in free state	41.5 °C (Zhang et al., 2018b)	R	Effective radius of MSMA sample	1.2 mm (Zhang et al., 2018a)
c	Damping coefficient	$10.1 \text{ kg} \cdot \text{s}^{-1}$	S	Cross-sectional area of MSMA sample	6 mm^2 (Zhang et al., 2018a)
c_0	Internal energy difference between austenite and martensite at 0 K	$1.0768 \times 10^7 \text{ J} \cdot \text{m}^{-3}$	T_0	Temperature of environment	20 °C
c_1	Entropy difference between austenite and martensite at 0 K	$3.4534 \times 10^4 \text{ J} \cdot \text{m}^{-3} \cdot \text{K}^{-1}$	t_h	Characteristic ambient heat-transfer time	0.1 s ~ 500 s
D_p	Threshold for phase transformation	$9.8422 \times 10^4 \text{ J} \cdot \text{m}^{-3}$	$z_0^{(0)}$	Initial volume fraction of austenite	0
E	Young's modulus of MSMA sample	50 GPa from mechanical tests in (Chen et al., 2013)	$z_1^{(0)}$	Initial volume fraction of martensite variant 1	1
f_{strain}	Frequency of output strain	120 Hz ~ 400 Hz (Zhang et al., 2018a)	$z_2^{(0)}$	Initial volume fraction of martensite variant 2	0
k	Interaction parameter accounting for incompatibility among martensite variants	$1.09 \times 10^3 \text{ J} \cdot \text{m}^{-3}$	ε_0	Strain change due to martensite reorientation	5.8% (Heczko, 2005b)
k_0	Interaction parameter accounting for incompatibility between austenite and martensite	$2.3810 \times 10^4 \text{ J} \cdot \text{m}^{-3}$	ε_a	Strain change along long axis of pseudo-tetragonal martensite during martensitic phase transformation	1.9% (Heczko et al., 2002)

k_s	Spring stiffness	$5.5 \text{ N}\cdot\text{mm}^{-1}$ from tests in (Zhang et al., 2018a)	ε_c	Strain change along short axis of pseudo-tetragonal martensite during martensitic phase transformation	3.9% (Heczko et al., 2002)
L	Linear coefficient	$1 \times 10^{-4} \text{ m}\cdot\text{s}\cdot\text{kg}^{-1}$	λ	Specific heat per unit volume	$4 \times 10^6 \text{ J}\cdot\text{m}^{-3}\cdot\text{K}^{-1}$ (Zhang et al., 2018a)
l_0	Initial length of MSMA sample	15 mm (Zhang et al., 2018a)	$\mu_0 H_{amp}^{app}$	Amplitude of applied magnetic field	0.78 T (Zhang et al., 2018a)
m	Mass of the moving parts in MSMA dynamic system	22.5 g from tests in (Zhang et al., 2018a)	σ_0	Initial compressive stress	0.4 MPa (Zhang et al., 2018a)

* The MSMA sample in (Zhang et al., 2018a) is rectangular with the dimensions of $15 \times 2 \times 3 \text{ mm}^3$ (respectively along x -, y - and z -axis in Fig. 4(a)) and the magnetic field is applied along the 2-mm edge. Using the formula for the volume average demagnetization factors of rectangular prisms in (Aharoni, 1998), we calculate the demagnetization factor of the $15 \times 2 \times 3$ rectangular prism in the 2-edge direction as: $N = 0.55$.

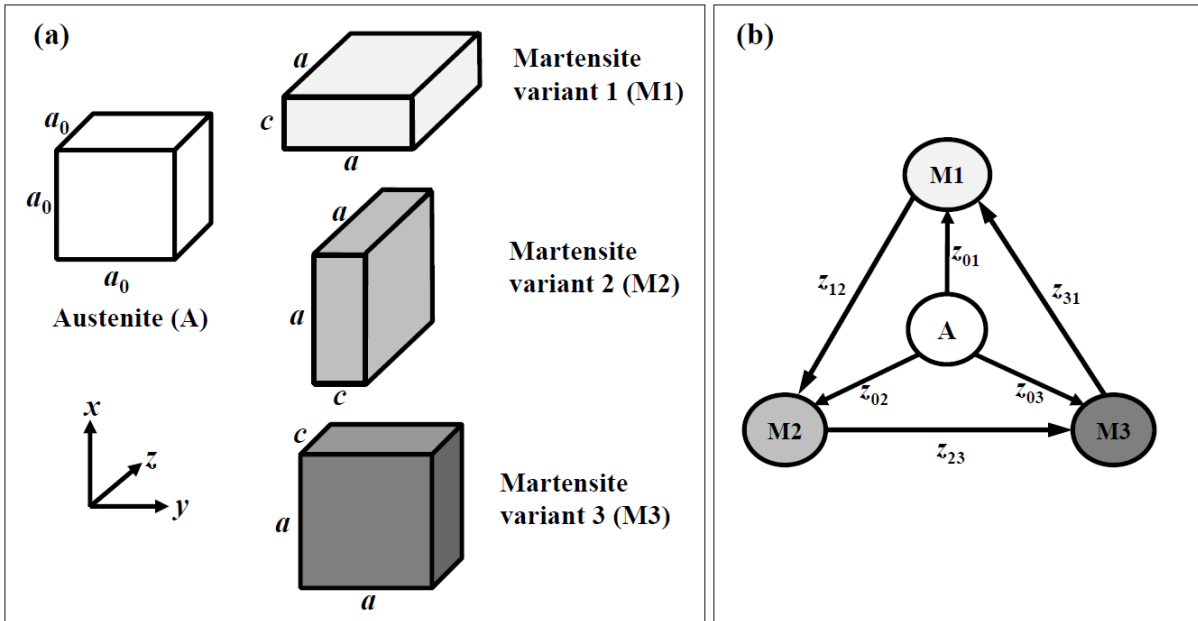


Fig. 1. (a) Schematic diagram of the austenite and the martensite variants of magnetic shape memory alloys. a_0 denotes the length of the austenite lattice; a and c denote the lengths of the long and short axes of the pseudo-tetragonal martensite lattice. The difference between a and c is exaggerated in the figure. (b) Martensite reorientation among three martensite variants (M1, M2, M3) and phase transformation between austenite (A) and martensite (M).

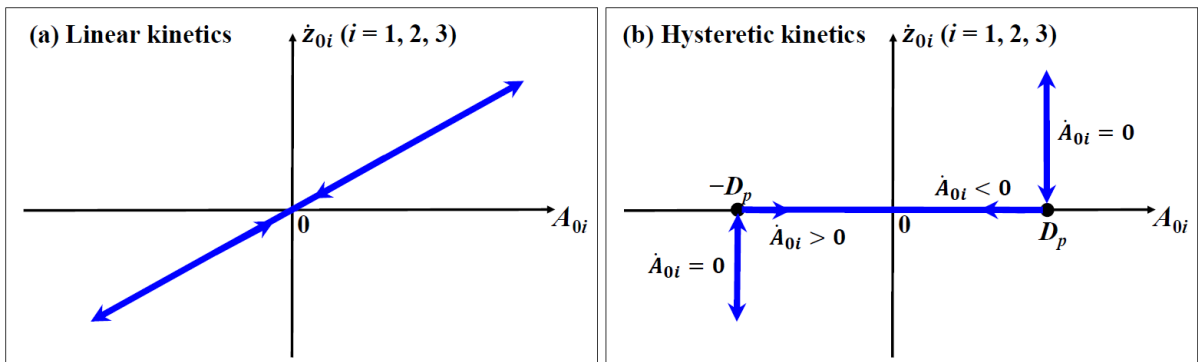


Fig. 2. Kinetic relation between the transformation rate \dot{z}_{0i} ($i = 1, 2, 3$) and the corresponding thermodynamic force A_{0i} for the phase transformation between austenite and martensite variant i : (a) linear phase transformation kinetics (no hysteresis), (b) phase transformation with threshold D_p , which results in hysteresis.

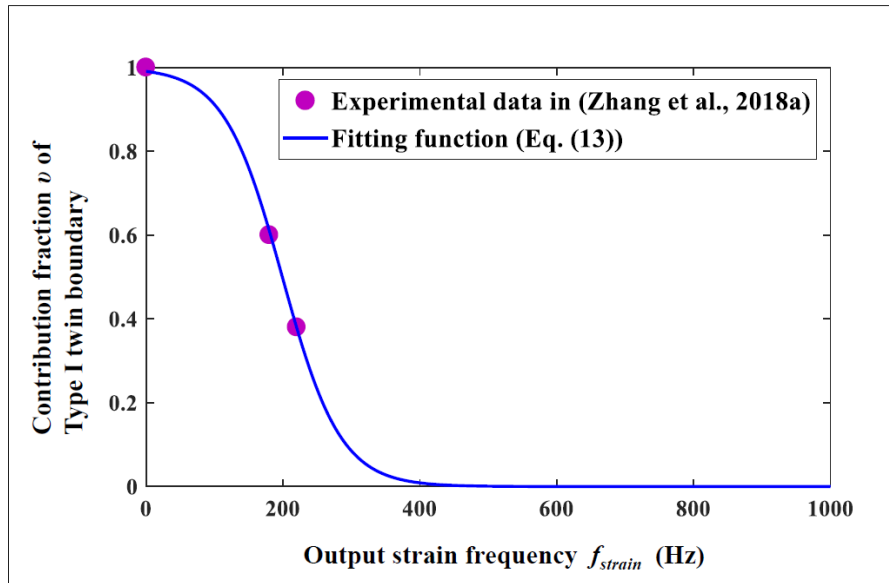


Fig. 3. Contribution fraction v of Type I twin boundary at different levels of output strain frequency f_{strain} .

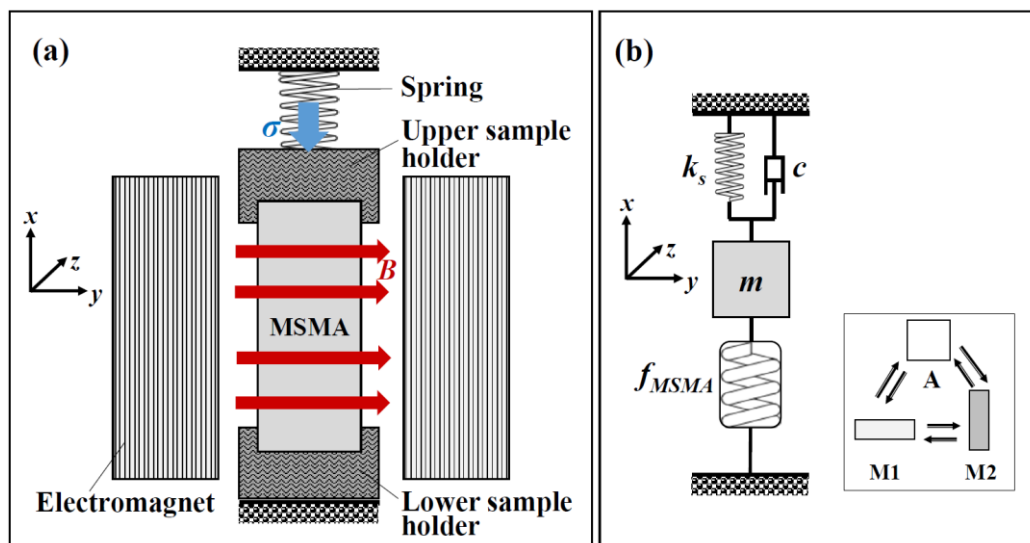


Fig. 4. (a) Experimental setup in (Zhang et al., 2018a). σ is the compressive stress applied by the spring and B is the magnetic flux density passing through the MSMA sample. (b) Mass-spring model of the dynamic MSMA system. Martensite reorientation between variant 1 (M1) and 2 (M2) and phase transformation between austenite (A) and martensite (M1 & M2) are induced during the experiments.

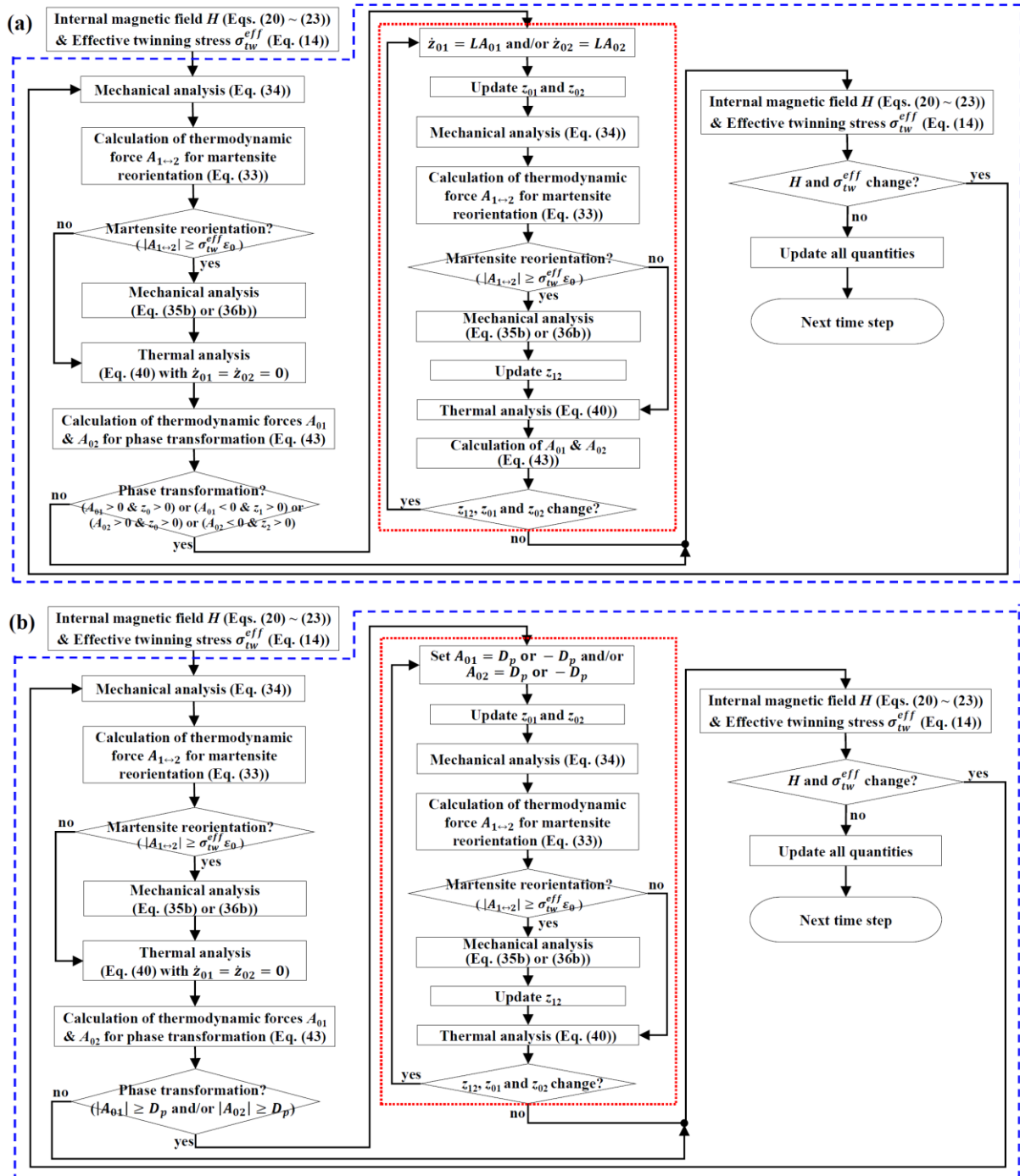


Fig. 5. Flowchart for each time step: (a) linear phase transformation kinetics (no hysteresis), (b) phase transformation with threshold (hysteresis). The dotted rectangle indicates an inner loop for the coupled martensite reorientation and phase transformation processes, and the dashed lines enclose an outer loop for the coupled thermo-magneto-mechanical analysis.

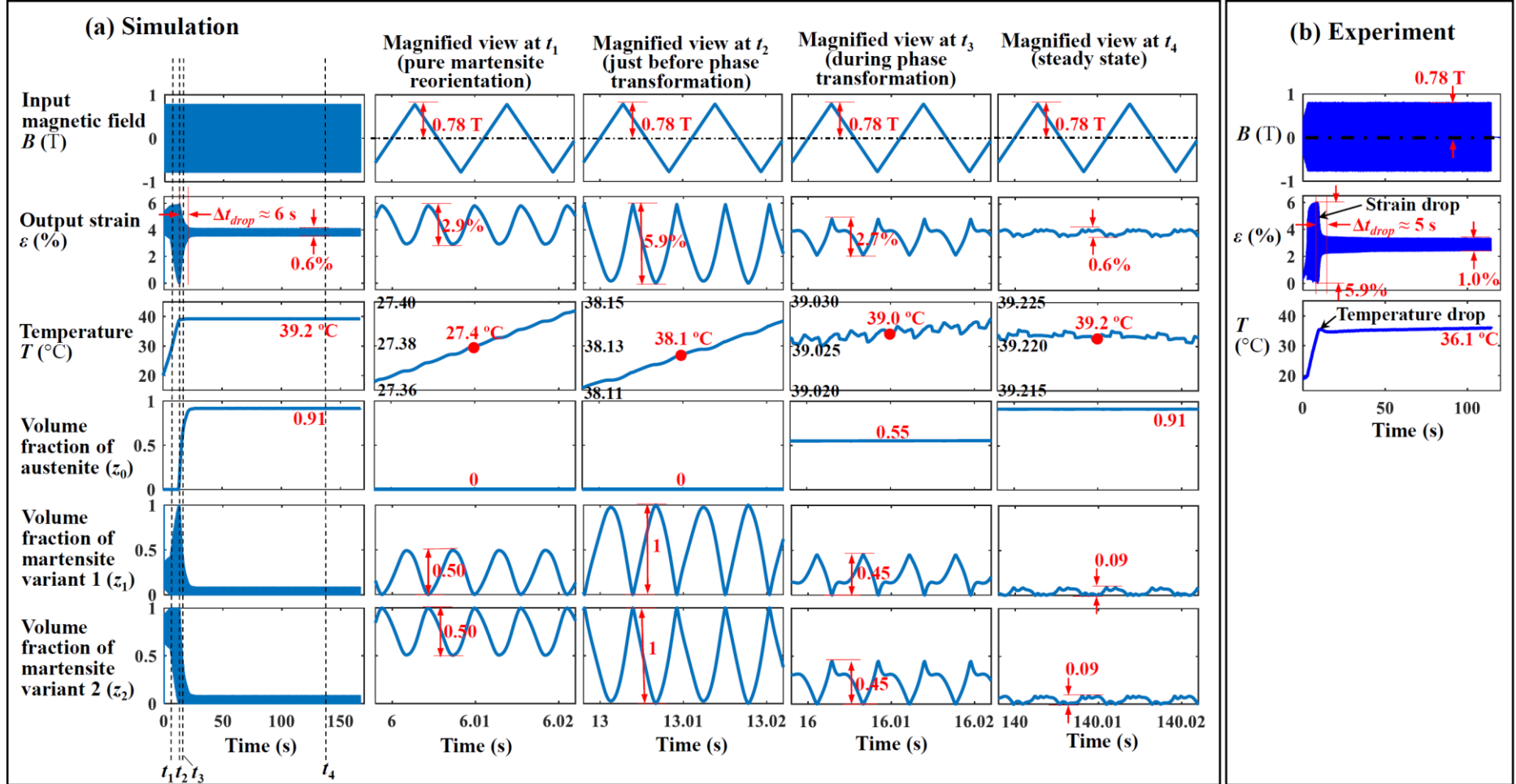


Fig. 6. A typical dynamic evolution of the magnetic-field-induced deformation in a Ni-Mn-Ga shape memory alloy: (a) simulation results, (b) experimental observations from (Zhang et al., 2018a). The experiment is conducted at the same loading condition as the simulation, i.e. $f_{strain} = 180$ Hz, $\sigma_0 = 0.4$ MPa, $T_0 = 20$ °C and airflow velocity $v_{air} = 0$ (corresponding to $t_h = 68.9$ s). While the simulated evolutions of strain and temperature agree with the experimental observation, the simulated evolutions of the internal variables (i.e. volume fractions of austenite (z_0) and martensite variants (z_1, z_2)) imply the physical mechanisms governing the experimentally-observed quantities (i.e. strain ε and temperature T).

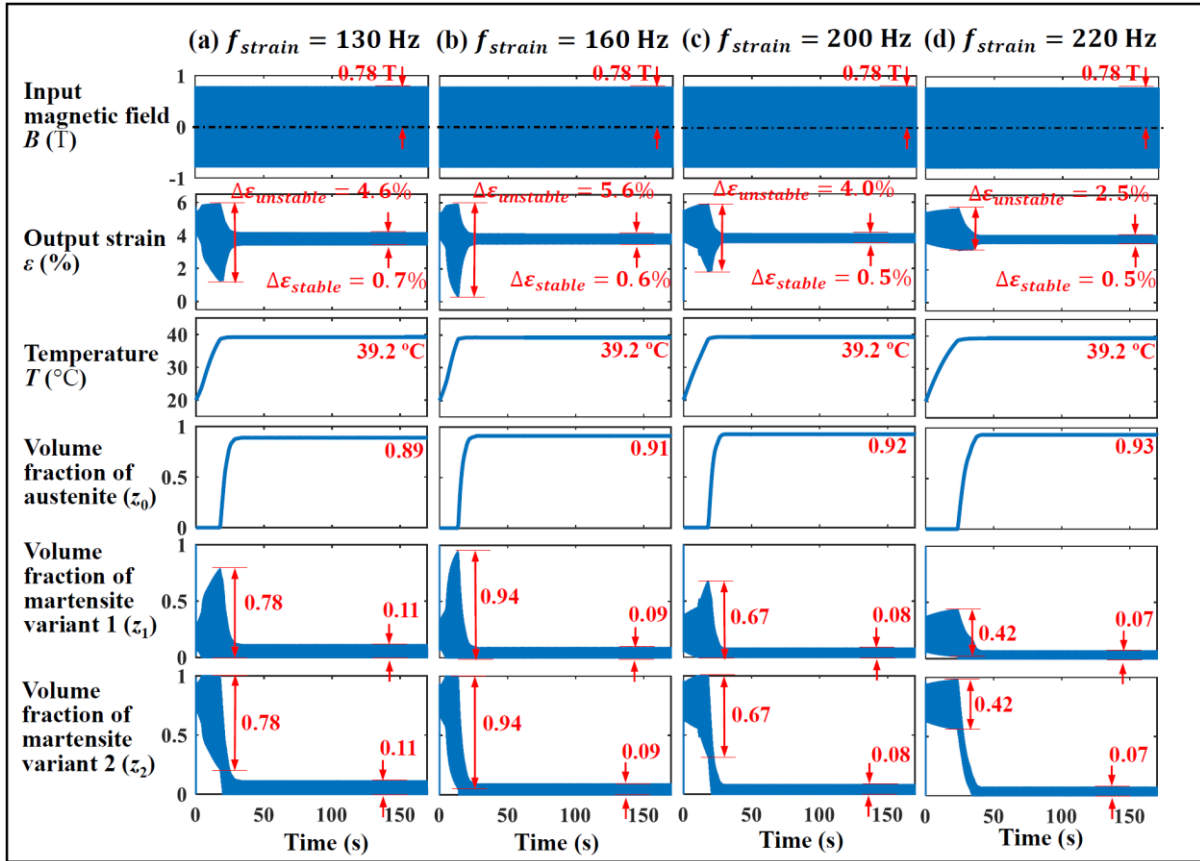


Fig. 7. Simulated dynamic evolution of the magnetic-field-induced deformation at different output strain frequencies: (a) $f_{strain} = 130$ Hz, (b) $f_{strain} = 160$ Hz, (c) $f_{strain} = 200$ Hz, (d) $f_{strain} = 220$ Hz. All simulations are conducted at the initial compressive stress $\sigma_0 = 0.4$ MPa, the characteristic ambient heat-transfer time $t_h = 68.9$ s, and the environmental temperature $T_0 = 20$ °C. While the strain amplitude $\Delta\epsilon_{unstable}$ of pure martensite reorientation (i.e. just before the phase transformation) depends on the frequency f_{strain} , the steady-state $\Delta\epsilon_{stable}$ and T_{stable} hardly depend on f_{strain} (e.g. $T_{stable} \approx 39.2$ °C for all the frequencies in the figure).

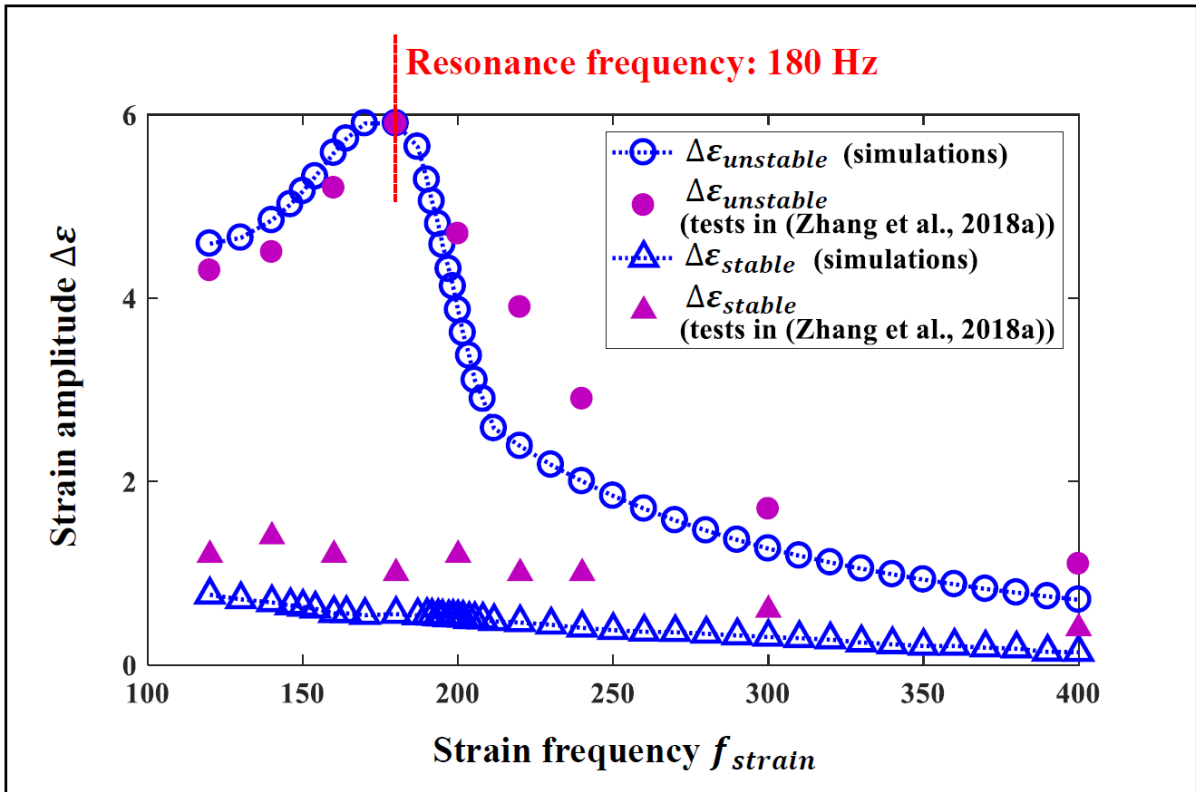


Fig. 8. Frequency effects on the stable and the unstable strain amplitudes, i.e. the strain amplitudes before and after the martensite-to-austenite phase transformation (strain drop), respectively. Simulations are conducted at the initial compressive stress $\sigma_0 = 0.4$ MPa, the characteristic ambient heat-transfer time $t_h = 68.9$ s and the environmental temperature $T_0 = 20$ °C. Experimental results from (Zhang et al., 2018a) are shown by solid symbols.

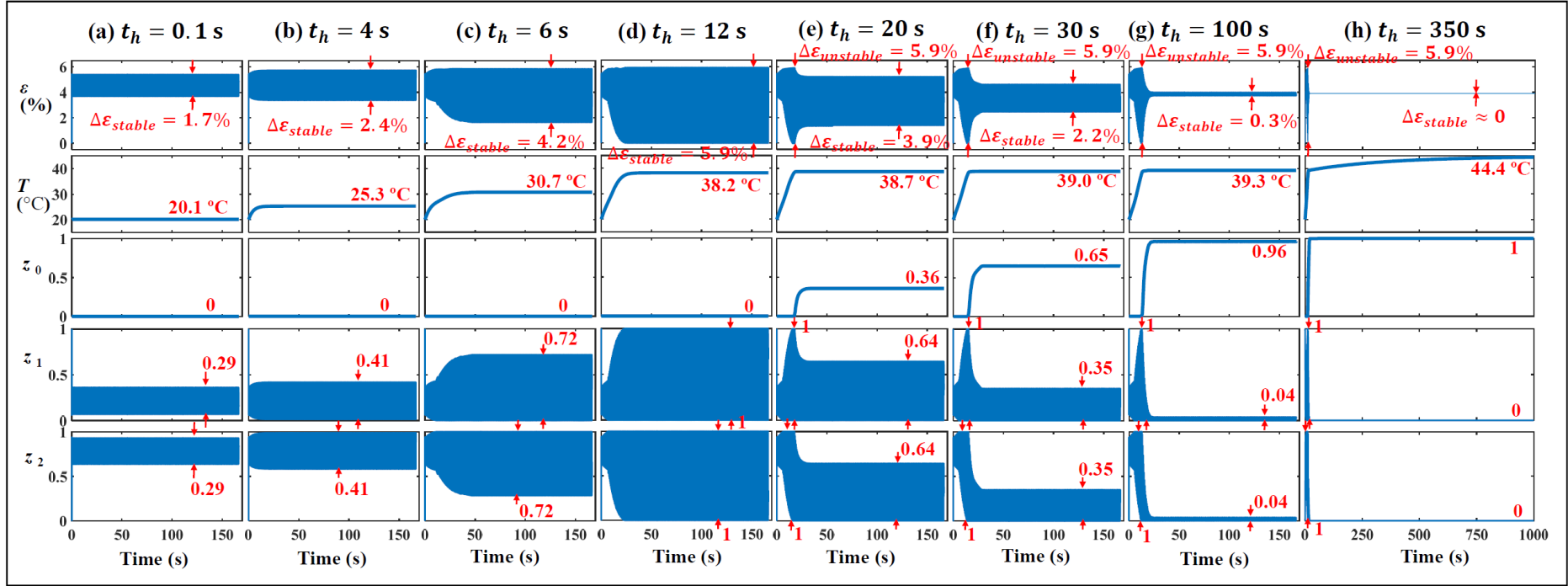


Fig. 9. The simulated evolutions of strain ε , temperature T , volume fraction z_0 of austenite, volume fraction z_1 of martensite variant 1 and volume fraction z_2 of martensite variant 2 under different ambient heat exchange conditions. The characteristic ambient heat-transfer time t_h changes from 0.1 s to 350 s, mimicking the ambient thermal condition from isothermal state to nearly adiabatic state. All simulations are conducted at the output strain frequency $f_{strain} = 180$ Hz, the initial compressive stress $\sigma_0 = 0.4$ MPa, and the environmental temperature $T_0 = 20$ °C.

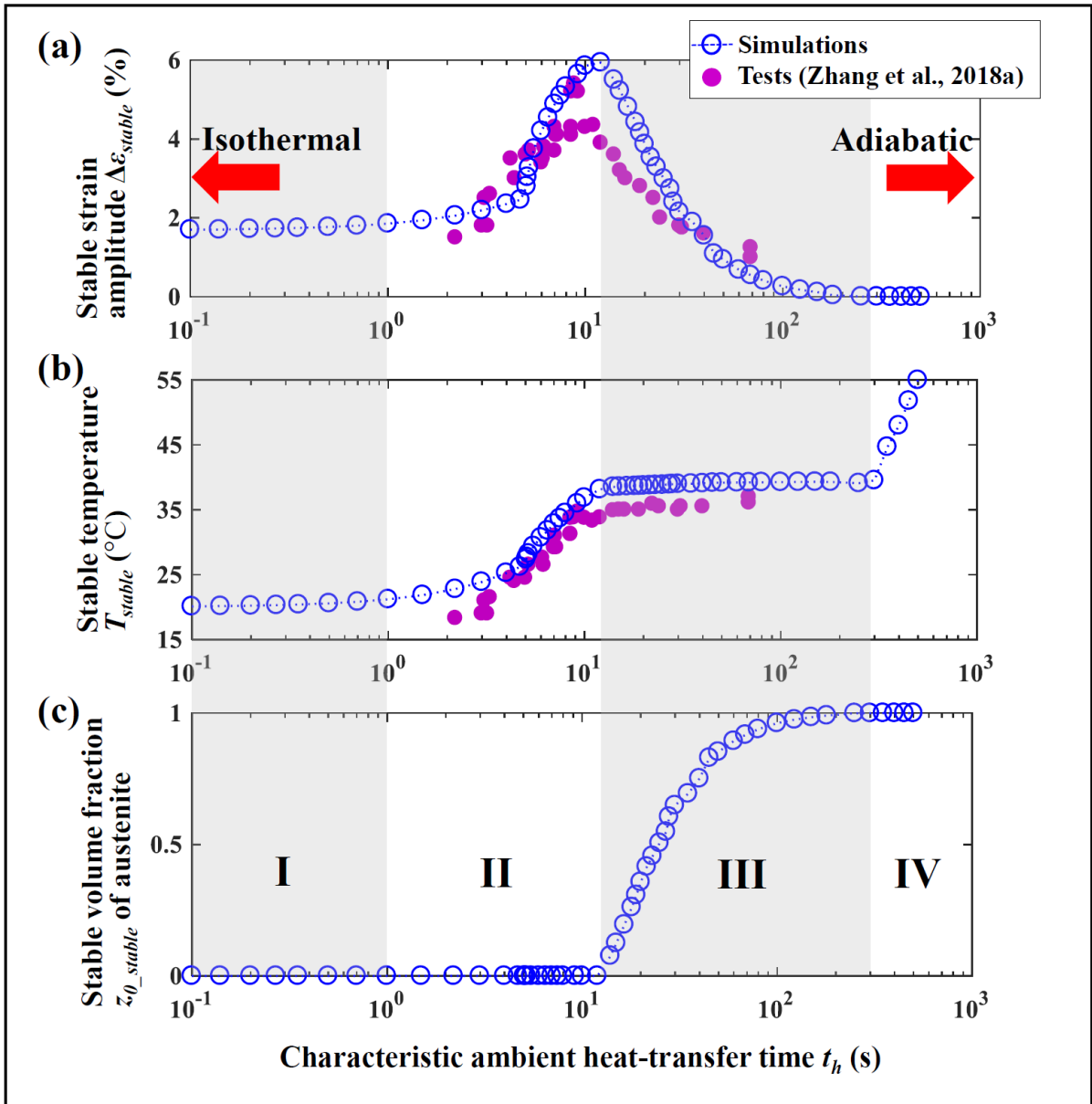


Fig. 10. Stable strain amplitude $\Delta\varepsilon_{stable}$ (a), stable temperature T_{stable} (b), and stable volume fraction z_{0_stable} of austenite (c) at different levels of the characteristic ambient heat-transfer time t_h . All simulations are conducted at the output strain frequency $f_{strain} = 180$ Hz, the initial compressive stress $\sigma_0 = 0.4$ MPa and the environmental temperature $T_0 = 20$ °C. Solid circles are the experimental results from (Zhang et al., 2018a).

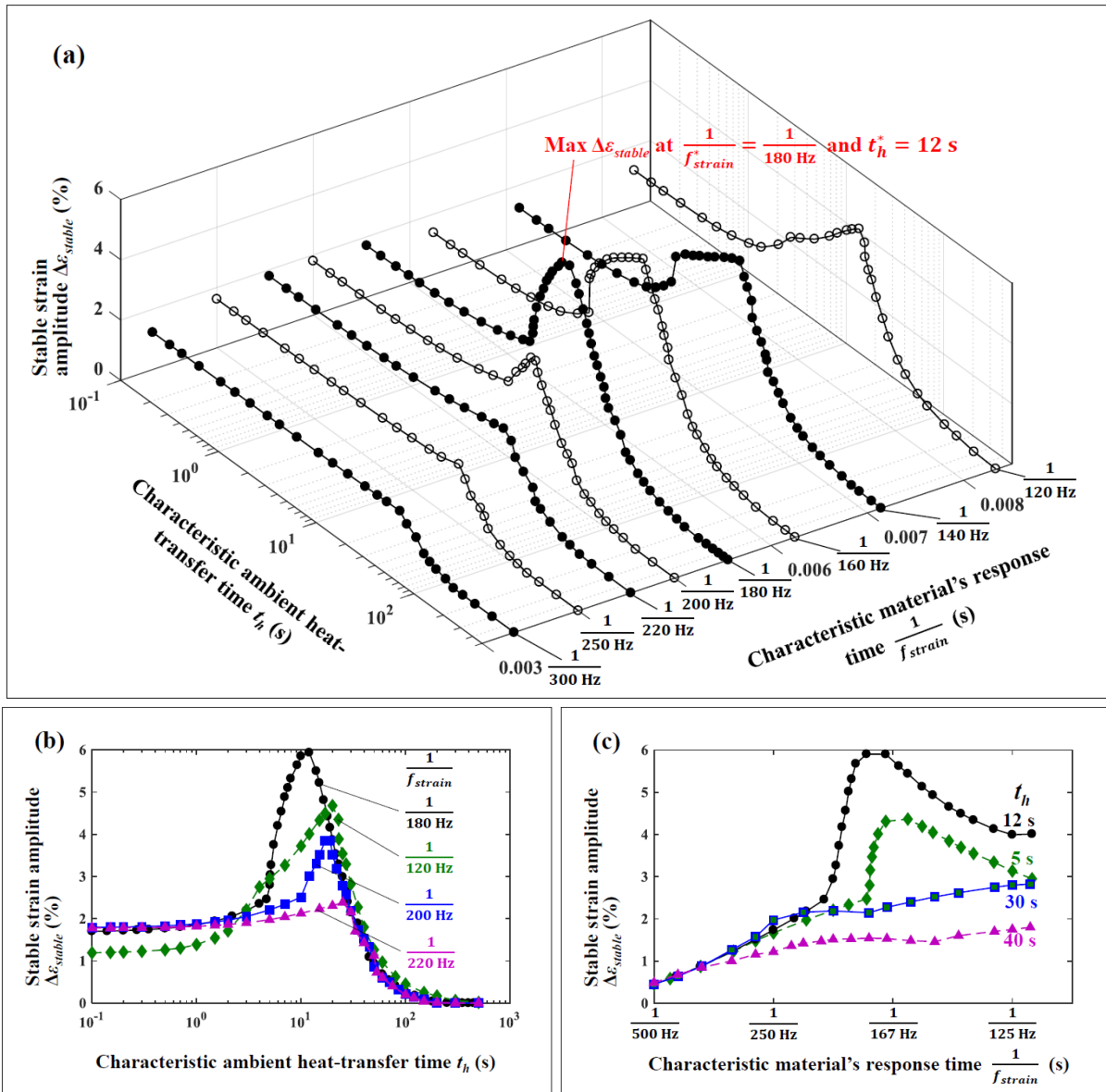
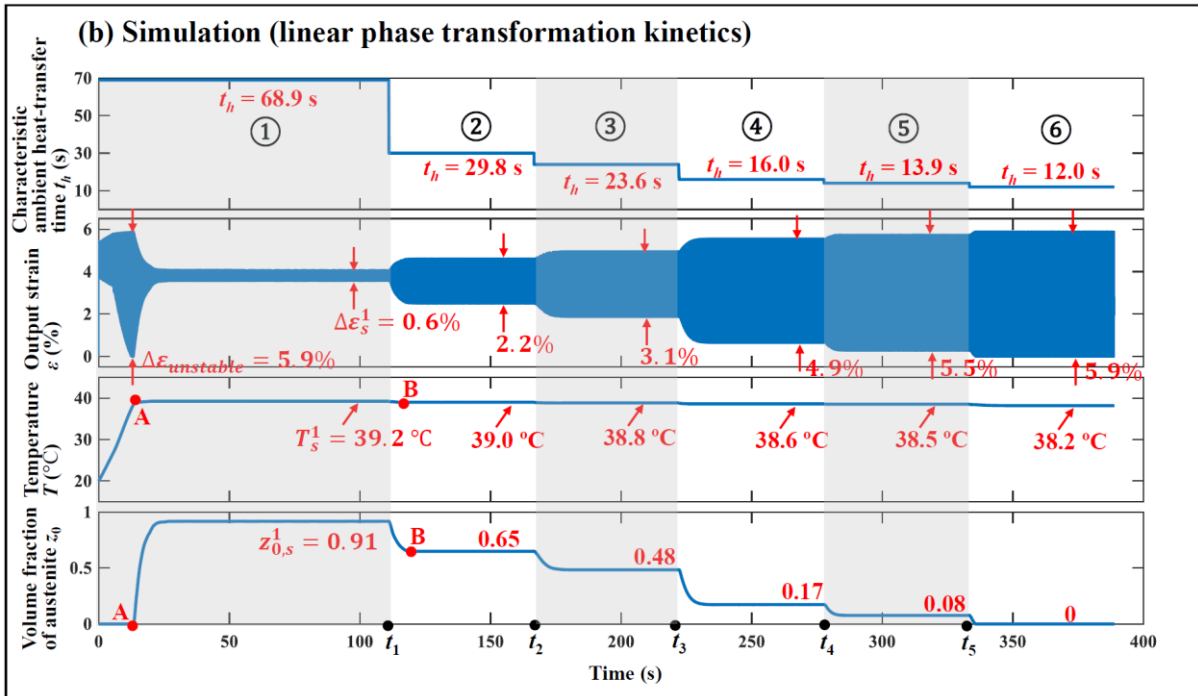
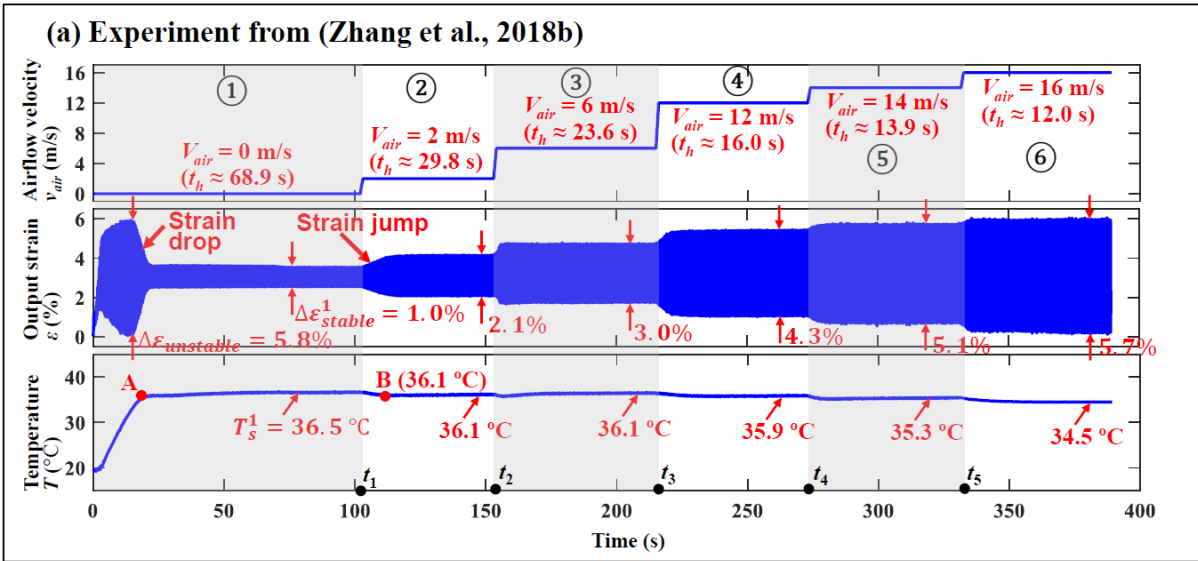


Fig. 11. Stable strain amplitude at two time scales: the characteristic ambient heat-transfer time t_h and the characteristic material's response time $\frac{1}{f_{strain}}$. (a) for a global 3D view; (b) and (c) for 2D views.



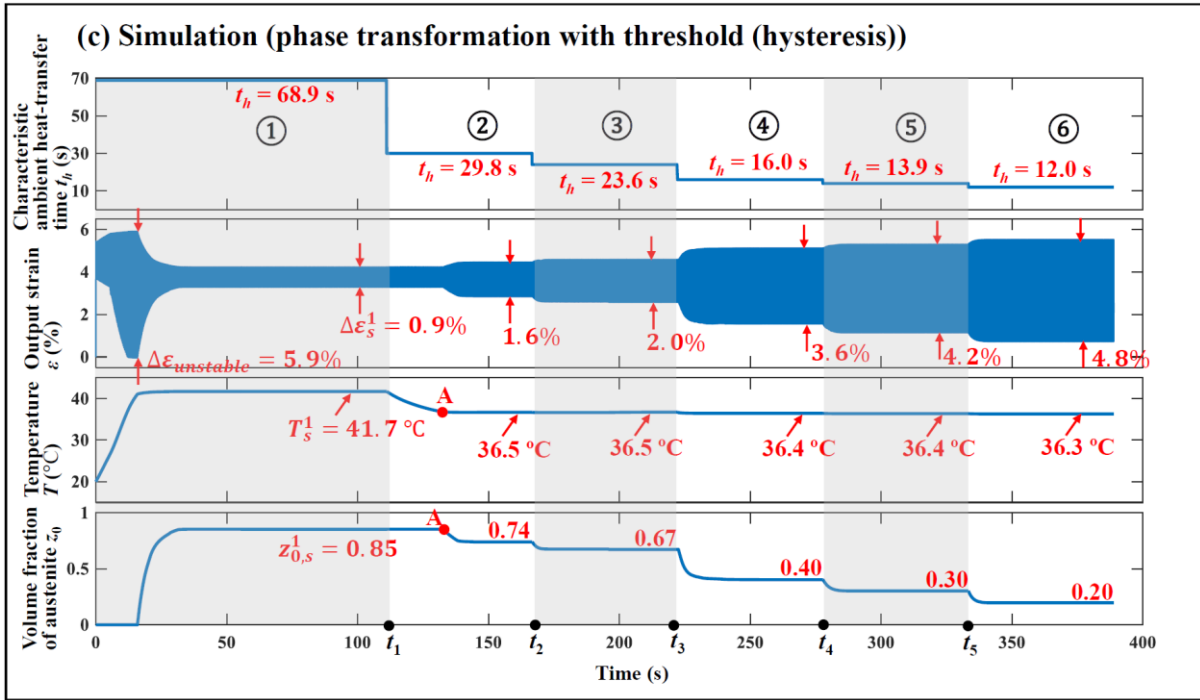


Fig. 12. Material's responses under varying heat transfer condition: (a) experimental observation from (Zhang et al., 2018b), (b) simulation using the linear phase transformation kinetics (no hysteresis), (c) simulation using the hysteretic phase transformation kinetics.

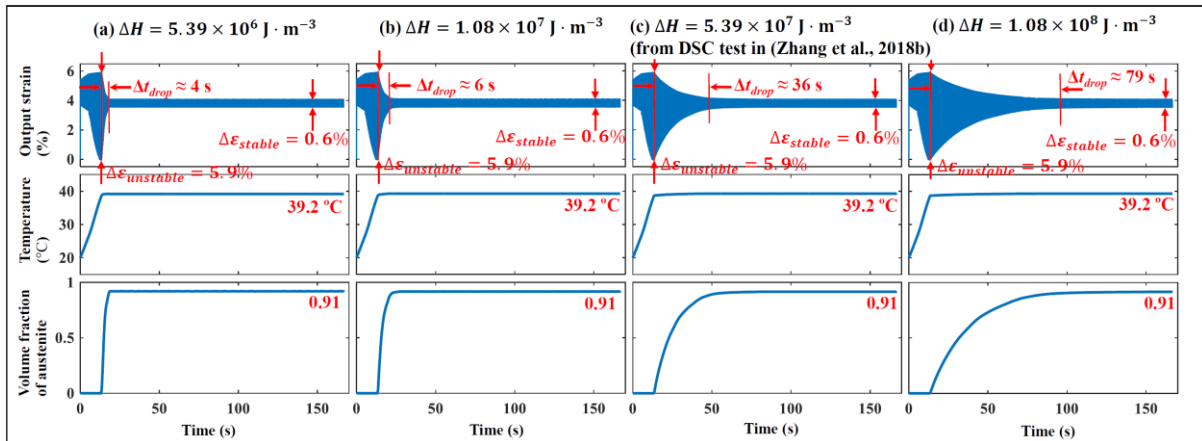


Fig. 13. Simulations of material's responses at different levels of latent heat ΔH : (a) $\Delta H = 5.39 \times 10^6 \text{ J} \cdot \text{m}^{-3}$, (b) $\Delta H = 1.08 \times 10^7 \text{ J} \cdot \text{m}^{-3}$, (c) $\Delta H = 5.39 \times 10^7 \text{ J} \cdot \text{m}^{-3}$ (from DSC test in (Zhang et al., 2018b)), (d) $\Delta H = 1.08 \times 10^8 \text{ J} \cdot \text{m}^{-3}$. All simulations are conducted at the output strain frequency $f_{strain} = 180 \text{ Hz}$, the initial compressive stress $\sigma_0 = 0.4 \text{ MPa}$, the characteristic ambient heat-transfer time $t_h = 68.9 \text{ s}$, and the environmental temperature $T_0 = 20 \text{ }^\circ\text{C}$.

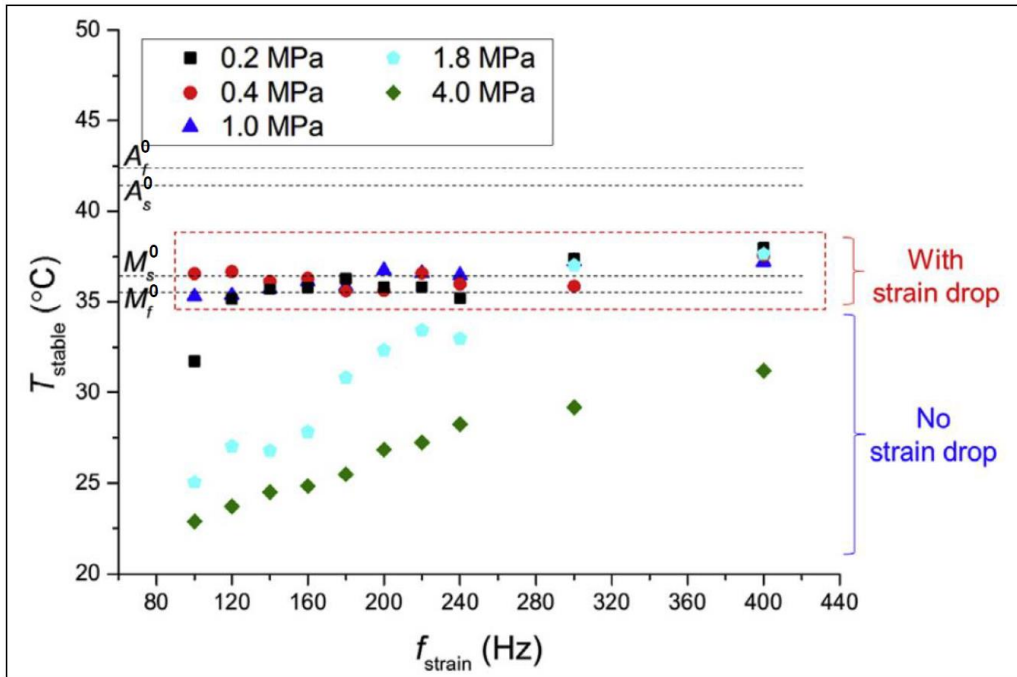


Fig. 14. Measured stable temperatures at different levels of strain frequency and initial compressive stress from (Zhang et al., 2018a). In all the tests where strain drop (M→A phase transformation) takes place, the stable temperature after the strain drop is close to M_s^0 and M_f^0 , but far from A_s^0 and A_f^0 .